nature communications

Article

https://doi.org/10.1038/s41467-024-54469-7

Regulating copper homeostasis of tumor cells to promote cuproptosis for enhancing breast cancer immunotherapy

Received: 3 November 2023

Accepted: 8 November 2024

Meng Guan[1,5], Kai Cheng[1,2,5], Xiao-Ting Xie[1,5], Yong Li[1], Meng-Wen Ma[1], Bin Zhang[1], Si Chen[3], Wei Chen[1], Bo Liu[1], Jin-Xuan Fan[1] & Yuan-Di Zhao[1,2,4]

Cuproptosis is an emerging mode of programmed cell death for tumor suppression but sometimes gets resisted by tumor cells resist under specific mechanisms. Inhibiting copper transporter ATPase (ATP7A) was found to disrupt copper ion homeostasis, thereby enhancing the effect of cuproptosis and eventually inhibiting tumor invasion and metastasis. In this study, we develop a multifunctional nanoplatfrom based on Cu_9S_8 (CAPSH), designed to enhance cuproptosis in tumor cells by specifically targeting ATP7A interference, while combining thermodynamic therapy with immune effects. The release of copper ions from CAPSH and the copper homeostasis interference by siRNA cooperatively increases the concentration of copper ions in tumor cells, which induces effectively cuproptosis and activates immune responses for suppressing development and metastasis of tumor. This nanoplatform simultaneously regulates cuproptosis from both principles of onset and development, facilitating the application of cuproptosis in tumor therapy.

Programmed cell death is a regulated process of cell death, including apoptosis, necrosis, pyroptosis, and ferroptosis[1,2]. As an emerging programmed cell death, cuproptosis is caused by copper-dependent mitochondrial dysfunction[3], whose key triggering factor is the accumulation of copper ions in cells[4]. It directly binds to the lipoylated components in the tricarboxylic acid (TCA) cycle, leading to the aggregation of lipoylated mitochondrial proteins and the disappearance of Fe-S cluster proteins, thereby inducing protein toxicity stress and ultimately leading to cell death[5,6]. Such direct ion-induced cell death has good controllability and precision, which is helpful for application in tumor therapy. However, the special mechanisms of copper transport and homeostasis in most tumor cells maintain a low concentration of copper homeostasis in the cytoplasm, thus resisting them from undergoing copper-induced death[7]. Specifically, copper transporter proteins represented by ATPase copper transporting alpha (ATP7A), are able to pump excess copper ions to the extracellular compartment, while ATP7A also regulates lysyl oxidase (LOX) activity thereby participating in the process of tumor invasion and metastasis[8]. Hence, the inhibition of ATP7A expression serves as an effective strategy to perturb the copper transport mechanism and homeostasis, ultimately leading to an increase in intracellular copper ions concentration and the inhibition of tumor development[9]. As a promising gene regulation technology for tumor therapy, small interfering RNA (siRNA) offers precise and selective targeting of a specific gene's mRNA while preserving the normal cellular function[10,11]. However, the precise delivery of siRNA in tumor cells faces significant challenges due to its

---

[1]Britton Chance Center for Biomedical Photonics at Wuhan National Laboratory for Optoelectronics - Hubei Bioinformatics & Molecular Imaging Key Laboratory, Department of Biomedical Engineering, College of Life Science and Technology, Huazhong University of Science and Technology, Wuhan 430074 Hubei, P. R. China. [2]Key Laboratory of Biomedical Photonics (HUST), Ministry of Education, Huazhong University of Science and Technology, Wuhan 430074 Hubei, P. R. China. [3]Hubei Key Laboratory of Plasma Chemistry and Advanced Materials, School of Material Science and Engineering, Wuhan Institute of Technology, Wuhan 430205 Hubei, P. R. China. [4]NMPA Research Base of Regulatory Science for Medical Devices & Institute of Regulatory Science for Medical Devices, Huazhong University of Science and Technology, Wuhan 430074 Hubei, P. R. China. [5]These authors contributed equally: Meng Guan, Kai Cheng, Xiao-Ting Xie. ✉e-mail: lbyang@mail.hust.edu.cn; jxfan@hust.edu.cn; zydi@mail.hust.edu.cn

inability to spontaneously traverse cell membranes, low bioavailability, and susceptibility to degradation by nucleases, thereby hindering its clinical applicability[12]. Nanocarriers offer several advantages in addressing the siRNA delivery challenge, encompassing highly controlled loading, protection of siRNA from degradation, and precise targeted delivery, among others[13]. A range of nano-delivery systems, including nanoparticles, liposomes, and viral vectors, has been devised to tackle the siRNA delivery issue[14,15]. Consequently, delivering siRNA via nanocarriers for the regulation of protein expression, such as ATP7A in tumor cells, can precisely disrupt their copper ions' metabolic homeostasis, thereby achieving the induction of cuproptosis in tumor cells[16].

As a versatile, easily prepared, and readily modifiable nano-delivery platform, Cu_9S_8 holds significant promise and advantages in the field of tumor gene therapy[17,18], including: (1) Cu_9S_8 is an excellent reservoir of copper ions in nano form, which is capable of releasing a large number of copper ions and triggering Cu death in tumor cells[19–21]; (2) Cu_9S_8 has a mesoporous structure, and its high specific surface area is conducive to cargo, especially siRNA loading, which can achieve the silencing of *ATP7A* gene, thus preventing the exocytosis of copper ions and further increasing the intracellular concentration of copper ions[22]; (3) Cu_9S_8 has a large number of Cu defects, which generates a localized surface plasmon resonance effect[23–25], and is able to absorb a large number of near-infrared region II (NIR-II) lasers (1064 nm) and undergo a strong photothermal conversion to kill the tumor cells. In comparison to visible light (390 nm-750 nm) and the near-infrared region I (NIR-I, 750–1000 nm), NIR-II excitation light offers superior tissue penetration depth, reduced light scattering, and lower absorption[26]. This makes it more suitable for the treatment of deep-seated tumors[27]. In summary, Cu_9S_8 represents a versatile nano-delivery system with the ability to integrate multiple therapeutic strategies, including copper-induced cell death, gene therapy, and photothermal therapy. It presents a more promising avenue for the development of effective tumor treatments[28–30].

In this work, we construct a multifunctional Cu_9S_8-based nanoplatform (CAPSH) to precisely target tumor tissues, effectively enhance cuproptosis by ATP7A interfering, and integrate thermodynamic therapy with immune effects (Fig. 1). CAPSH is supported by hollow mesoporous Cu_9S_8 nanoparticles, loaded with alkyl radical precursor 2,2-azobis[2-(2-imidazolin-2-yl)propane] dihydrochloride (AIPH), and coated with poly(arylene propylene amine) hydrochloride (PAH) to electrostatically adsorb siRNA (siATP7A). The outer layer is coated with hyaluronic acid (HA) to prevent siRNA degradation and provide tumor targeting. The hyaluronidase in the tumor microenvironment degrades HA to promote the endocytosis of CAPSH, and further releases AIPH, siATP7A, and a large amount of copper ions. Through 1064 nm laser irradiation, Cu_9S_8 undergoes photothermal conversion, induces tumor cell death upon heating, and decomposes

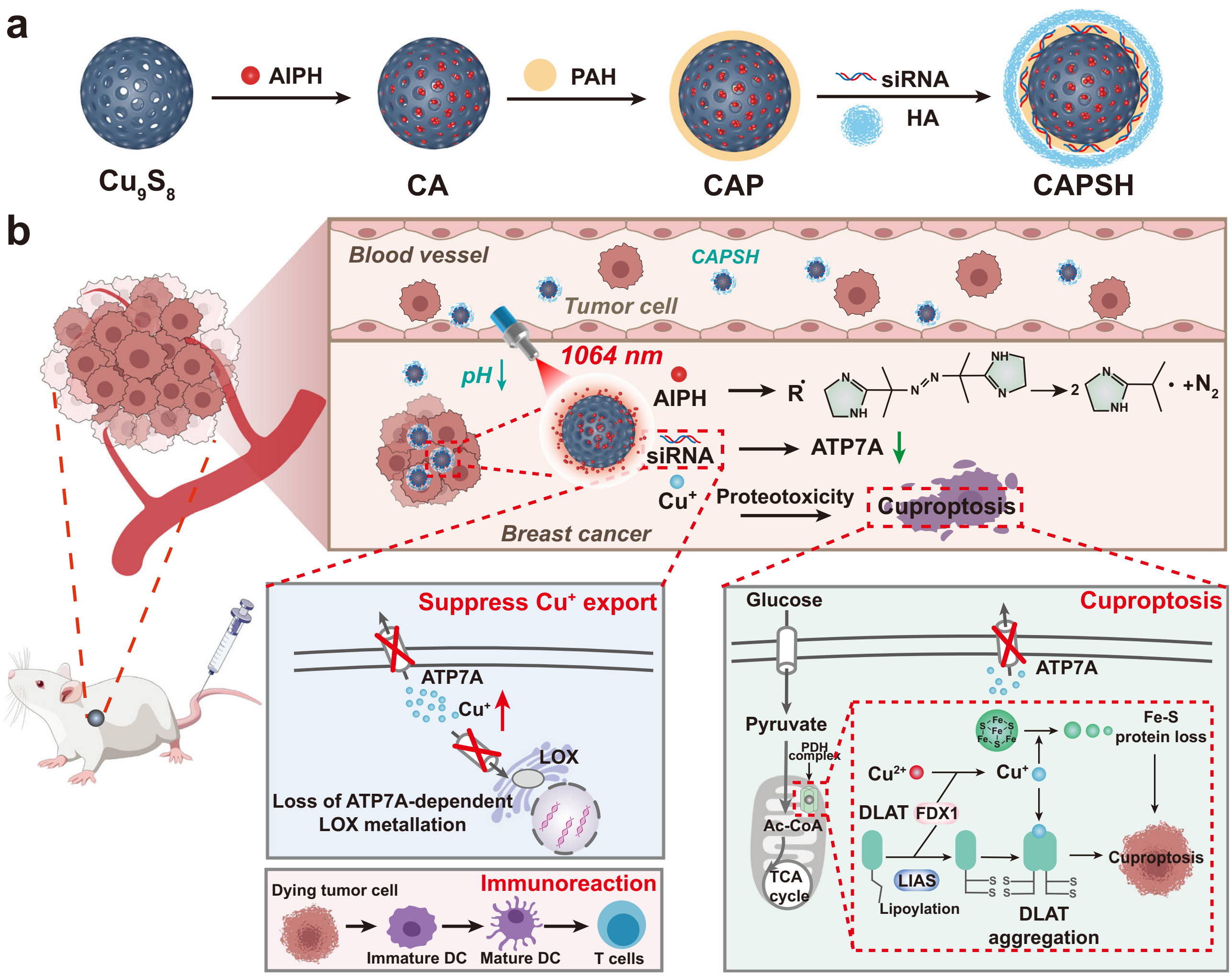

Fig. 1 | Synthesis and antitumor mechanism of CAPSH. a Schematic diagram of the synthesis of CAPSH. **b** Schematic diagram of copper sulfide-based nanocarriers for the regulation of copper homeostasis in tumors enabling synergistic treatment of breast cancer. Figure 1b was created with BioRender.com released under a Creative Commons Attribution 4.0 International license (https://creativecommons.org/licenses/by/4.0/).

AIPH to produce oxygen-independent alkyl radicals. siATP7A enhances cuproptosis and inhibits tumor metastasis by blocking copper ion efflux and suppressing LOX activity. Both in vivo and in vitro experiments verify that the copper death strategy mediated by CAPSH elicits a robust antitumor immune response, effectively curbing tumor growth and demonstrates its promising potential in cancer treatment[31–34].

Results

Synthesis and characterization of CAPSH

The synthetic scheme of CAPSH was shown in Fig. 1a. The preparation of Cu_9S_8 nanoparticles (NPs) was composed of synthesis and in situ sulfidation of Cu_2O. The synthesis method was optimized by characterizing the UV-vis absorption spectrum, hydrodynamic size, and zeta potential of Cu_9S_8 (Supplementary Figs. 1–4). The results obtained from transmission electron microscopy (TEM, Fig. 2a) and scanning electron microscopy (SEM, Supplementary Fig. 5) showed that the synthesized Cu_9S_8 NPs had a spherical and hollow mesoporous structure. The average diameter of the Cu_9S_8 NPs was ~100 nm, with a shell thickness of 20 nm. This unique structure was believed to be a result of the "Kirkendall effect" induced by sulfurization. The TEM image of CAPSH exhibited negligible alterations when compared to that of Cu_9S_8 NPs. The results of the TEM elemental mapping of CAPSH showed that the Cu and S elements had high signal intensities in the shell region and low signal intensities in the central cavity, which was consistent with the hollow structure of Cu_9S_8 NPs. Within CAPSH, alongside the presence of Cu and S elements, the emergence of elements such as N and P provided unequivocal confirmation of the effective encapsulation of both AIPH and siRNA (Fig. 2a).

The crystal structure of Cu_9S_8 NPs was investigated using an X-ray diffractometer (XRD, Fig. 2b). The results showed that Cu_9S_8 NPs had diffraction peaks at 29.3°, 31.9°, and 48.0°, which were consistent with the (0022), (1013), and (111) crystal planes of Yarrowite Cu_9S_8 (PDF#36-0379). This suggested that a non-stoichiometric copper sulfide with copper vacancies was produced. To demonstrate this, Cu_9S_8 NPs were tested for X-ray photoelectron spectroscopy (XPS, Fig. 2c, d). The coexistence of Cu^+ and Cu^{2+} suggests the formation of a non-stoichiometric copper sulfide. The UV-vis-NIR spectrophotometer was employed to examine the absorption spectra of Cu_2O and Cu_9S_8 NPs (Fig. 2e). The absorption band of Cu_9S_8 NPs exhibited a "V" shape

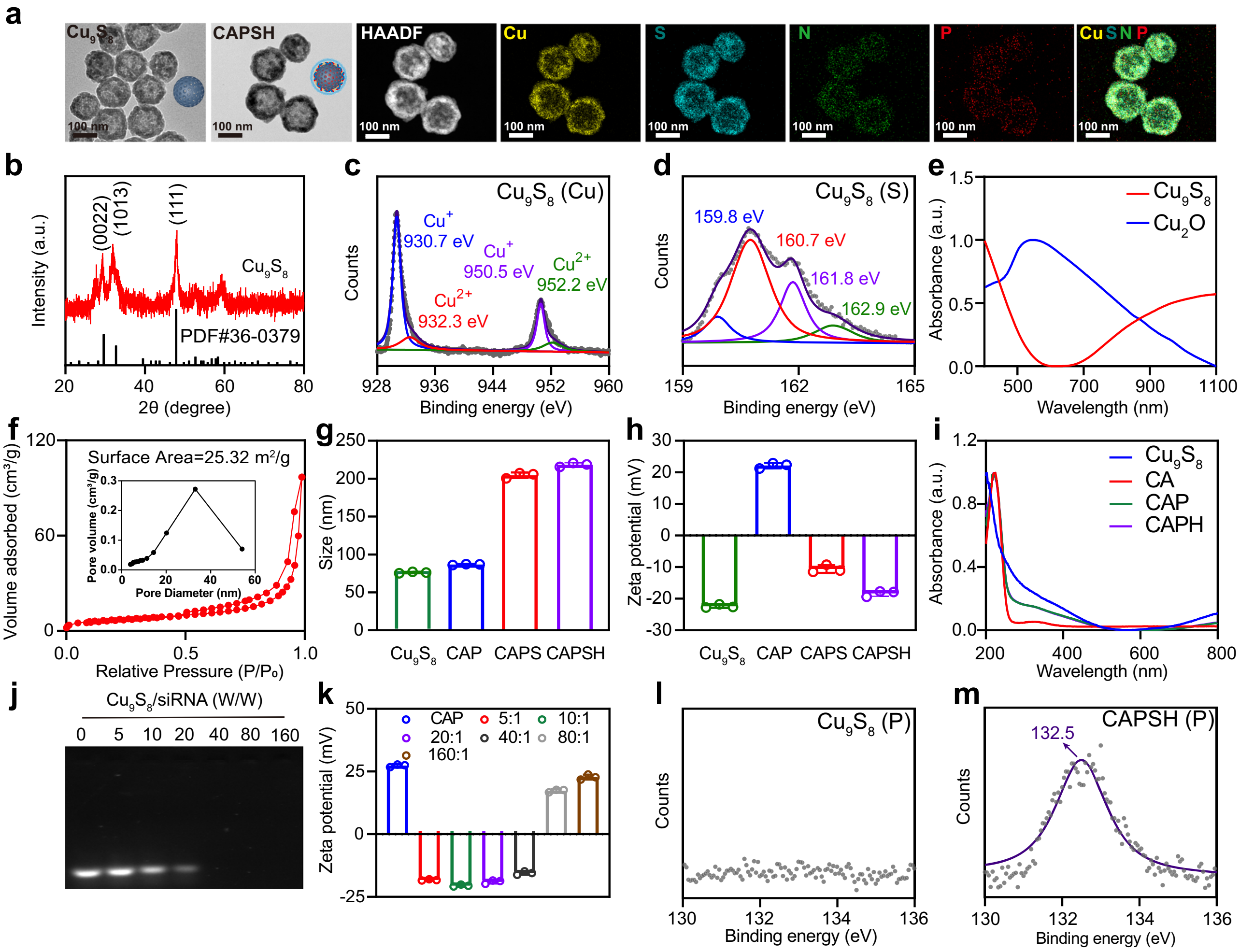

Fig. 2 | Characterization of CAPSH. a TEM images of Cu_9S_8 and CAPSH, along with an element mapping image of CAPSH. Images are representative of three independent experimental replicates. Scale bar: 100 nm. **b** XRD pattern of Cu_9S_8. **c**, **d** XPS energy spectra of elemental Cu and elemental S of Cu_9S_8. **e** UV-vis absorption spectra of Cu_9S_8 and Cu_2O. **f** Nitrogen adsorption and desorption curves and (illustration) pore size distribution of Cu_9S_8. **g** Hydration diameter of Cu_9S_8, CAP, CAPS, and CAPSH. Data were presented as the means ± SD ($n = 3$ independent experiments). **h** Zeta potential of Cu_9S_8, CAP, CAPS, and CAPSH. Data were presented as the means ± SD ($n = 3$ independent experiments). **i** UV-vis absorption spectra of Cu_9S_8, CA, CAP and CAPH. **j** Delayed determination of siRNA by agarose gel electrophoresis at different w/w ratios of Cu_9S_8 to siRNA. Images are representative of three independent experimental replicates. **k** Zeta potentials of Cu_9S_8 and siRNA with different w/w. Data were presented as the means ± SD ($n = 3$ independent experiments). **l** XPS energy spectra of elemental P of Cu_9S_8. **m** XPS energy spectra of elemental P of CAPS. Source data are provided as a Source Data file.

and notable absorption in the near-infrared area, in contrast to the continuous absorption band of Cu_2O. This phenomenon arises from the localized surface plasmon resonance effect (LSPR) correlated with copper vacancies present within the Cu_9S_8 NPs. Notably, the Cu_9S_8 dispersion exhibits comparatively enhanced absorbance within the NIR-II window compared to the NIR-I window. This heightened absorbance profile facilitates improved penetration into biological tissues, enabling the utilization of light within the NIR-II window for more effective excitation.

Through nitrogen adsorption-desorption experiments, the pore size distribution of Cu_9S_8 was analyzed (Fig. 2f). The results revealed a distinct hysteresis loop in the adsorption isotherm of copper sulfide, indicating the presence of mesopores with interconnected channels in the material. The specific surface area of Cu_9S_8 nanoparticles was calculated to be 25.3 m^2/g, and the pore diameter was 33.0 nm. Additionally, we performed small-angle XRD experiments (Supplementary Fig. 6; The detailed testing conditions are shown in Supplementary Table 1). The results showed diffraction peaks at low scattering angles (typically less than 5 degrees), further confirming the presence of mesoporous structures in the sample. To demonstrate the importance of mesoporous structures in improving drug loading capacity and therapeutic efficacy, we synthesized non-mesoporous CuS (Supplementary Fig. 7) and compared their drug loading capacity with that of hollow mesoporous Cu_9S_8. The results indicated that the drug loading capacity of hollow mesoporous Cu_9S_8 was 3.67 times higher than that of non-mesoporous CuS (Supplementary Fig. 8). A higher drug loading capacity can enhance therapeutic efficacy and reduce the frequency of administration.

The hydrodynamic size of Cu_9S_8 NPs and CAPSH was about 112.8 ± 2.0 nm and 218.2 ± 2.1 nm respectively, which further proved loading the drug (Fig. 2g). The surface charge of Cu_9S_8 NPs was changed from -22.4 ± 0.43 mV to 22.1 ± 0.71 mV after loading AIPH and PAH, demonstrating that the successful encapsulation of PAH facilitated the electrostatic adsorption of negatively charged siRNA. The surface charge further changed to -10.6 ± 0.98 mV and -18.3 ± 0.76 mV separately after additional loading of siRNA and encapsulation of HA-formed CAPSH (Fig. 2h). Comparison of the absorption spectra of Cu_9S_8 NPs, CA, CAP and CAPH (Fig. 2i), CA, CAP, and CAPH exhibited a prominent absorption peak at 220 nm after AIPH loading. The capacity of Cu_9S_8 NPs to load siRNA was confirmed through electrophoresis experiments using agarose gel (Fig. 2j). The outcomes indicated that Cu_9S_8 NPs was effective at loading siRNA at a mass ratio of 40:1 and beyond (Fig. 2k). As the mass ratio of Cu_9S_8 NPs to siRNA rose, the surface charge of CAPS underwent a gradual trend which first decreased and then increased. By comparing the XPS spectra of Cu_9S_8 NPs with CAPSH, it was further confirmed that siRNA was successfully loaded into Cu_9S_8 NPs. Since nucleotides and phosphates in siRNA molecules make up a significant portion of the P elements in siRNA, CAPSH possessed unique peaks in P spectra, while no P signals were found in Cu_9S_8 NPs (Fig. 2l, m). The XPS spectra of Cu and S elements in CAPSH exhibited no significant changes, indicating that the modifications with PAH and HA did not affect the structure of Cu_9S_8 NPs and the loading of siRNA (Supplementary Fig. 9).

Additionally, we conducted in vitro stability simulation experiments on CAPSH. CAPSH was co-incubated with H_2O, PBS, NaCl, DMEM, 1640, 10% fetal bovine serum (FBS), 50% FBS, and 100% FBS. No significant precipitation was observed in any of the solutions (Supplementary Fig. 10a). The hydrated particle size (Supplementary Fig. 10b), zeta potential (Supplementary Fig. 10c), and polydispersity index (PDI) (Supplementary Fig. 10d) in PBS, DMEM, and DMEM + 50% FBS showed no significant changes over 12 days. After soaking CAPSH in simulated body fluid, the pH values of the solution measured at different time points did not show significant changes, indicating that CAPSH has favorable chemical stability and biocompatibility. (Supplementary Fig. 10e).

In vitro performance evaluation of CAPSH

The photothermal properties of Cu_9S_8 were studied using a near-infrared thermal imaging camera. A range of Cu_9S_8 dispersion at concentrations of (0–100 μg/mL) were exposed to a 1064 nm laser (0.75 W/cm^2), while concurrently monitoring the temperature via an infrared camera (Fig. 3a, b). Under 1064 nm laser irradiation, the temperature of water increased by 12.5 °C in 300 s. The temperature of Cu_9S_8 dispersion (100 μg/mL) increased rapidly by 42.7 °C in 300 s and showed a concentration-dependent temperature increase of 30.9, 37.9, and 40.9 °C, respectively (the concentration of Cu_9S_8 dispersions were 12.5, 25, and 50 μg/mL). In addition, at the same concentration, the warming is more pronounced at higher power densities (Fig. 3c, d). The temperature profiles resulting from repeated laser exposure on Cu_9S_8 dispersions vividly illustrated the commendable stability of its photothermal characteristics (Fig. 3e). The time constant (τ) of Cu_9S_8 was 128.5 s (Fig. 3f). The photothermal conversion efficiency of Cu_9S_8 was calculated as 42.3% using the given equation. Moreover, the synthesized Cu_9S_8 displayed excellent photothermal performance, making it suitable for research on tumor photothermal therapy.

AIPH rapidly decomposes when exposed to heat and produces alkyl radicals. We utilized the photothermal effect of Cu_9S_8 to control the decomposition of AIPH. Next, the generated free radicals were detected by UV-vis and ESR spectroscopy. 2,2′-azinobis(3-ethylbenzothiazoline-6-sulfonic acid ammonium salt) (ABTS) could react with free radicals to form $ABTS^{+\bullet}$, which has characteristic absorption peaks in the 400–1000 nm range of the UV-vis absorption spectrum. The distinctive absorption peaks of $ABTS^{+\bullet}$ gradually intensified as the laser exposure time extended, indicating that the concentration of $ABTS^{+\bullet}$ was gradually increased by the generation of free radicals in the solution (Fig. 3g). The same conclusion was reached using methylene blue to detect reactive oxygen species (Supplementary Fig. 11). Additionally, we employed POBN to capture the free radicals generated by AIPH (Fig. 3h). The CAPH group exhibited distinct characteristic signals under laser irradiation. This further confirms that the photothermal effect of Cu_9S_8 could trigger the decomposition of AIPH and produce alkyl radicals.

Next, we investigated the release of AIPH and copper ions from CAPSH under acidic conditions. The drug release from CAPSH after 48 h was found to be $67.5 \pm 1.6\%$ at pH 5.4, while it was only $36.1 \pm 0.9\%$ at pH 7.4 (Fig. 3i). After replacing AIPH with DOX, the drug release capability in an acidic environment was further verified by detecting the fluorescence of DOX. The results of the UV-vis absorption spectra (Supplementary Fig. 12a) and fluorescence spectra (Supplementary Fig. 12b) showed that DOX-loaded Cu_9S_8 exhibited the same characteristic absorption peaks and fluorescence emission peaks as DOX. This phenomenon clearly confirms the successful loading of DOX onto Cu_9S_8. The release experiment results indicated that DOX was significantly released under acidic conditions. This finding further demonstrates the ability of CAPSH to release drugs in an acidic environment (Supplementary Fig. 13). Inductively Coupled Plasma Mass Spectrometry (ICP-MS) analysis of CAPSH's ability to release copper ions under acidic conditions can be found in Fig. 3j, revealing that the release of copper ions was 2964.4 ± 55.2 μg/L at pH 5.4, while the release was only 941.8 ± 26.9 μg/L at pH 7.4. The characteristic of CAPSH to release AIPH and copper ions in response to acidic conditions contributed to minimizing the potential cytotoxicity to healthy tissues.

Cytotoxicity and combined therapy in vitro

The impact of CPH (Cu_9S_8-clad PAH and HA) on the survival of 4T1 cells was analyzed through MTT (Fig. 4a). After incubating 4T1 cells with CPH at concentrations ranging from 0 to 60 μg/mL for 24 h, the viability of all cells remained above 95%. However, when the concentration was increased to 100 μg/mL, the survival rate dropped significantly to only 48.4%, which demonstrated the high biocompatibility of CPH at low concentrations. Two concentrations, 40 and

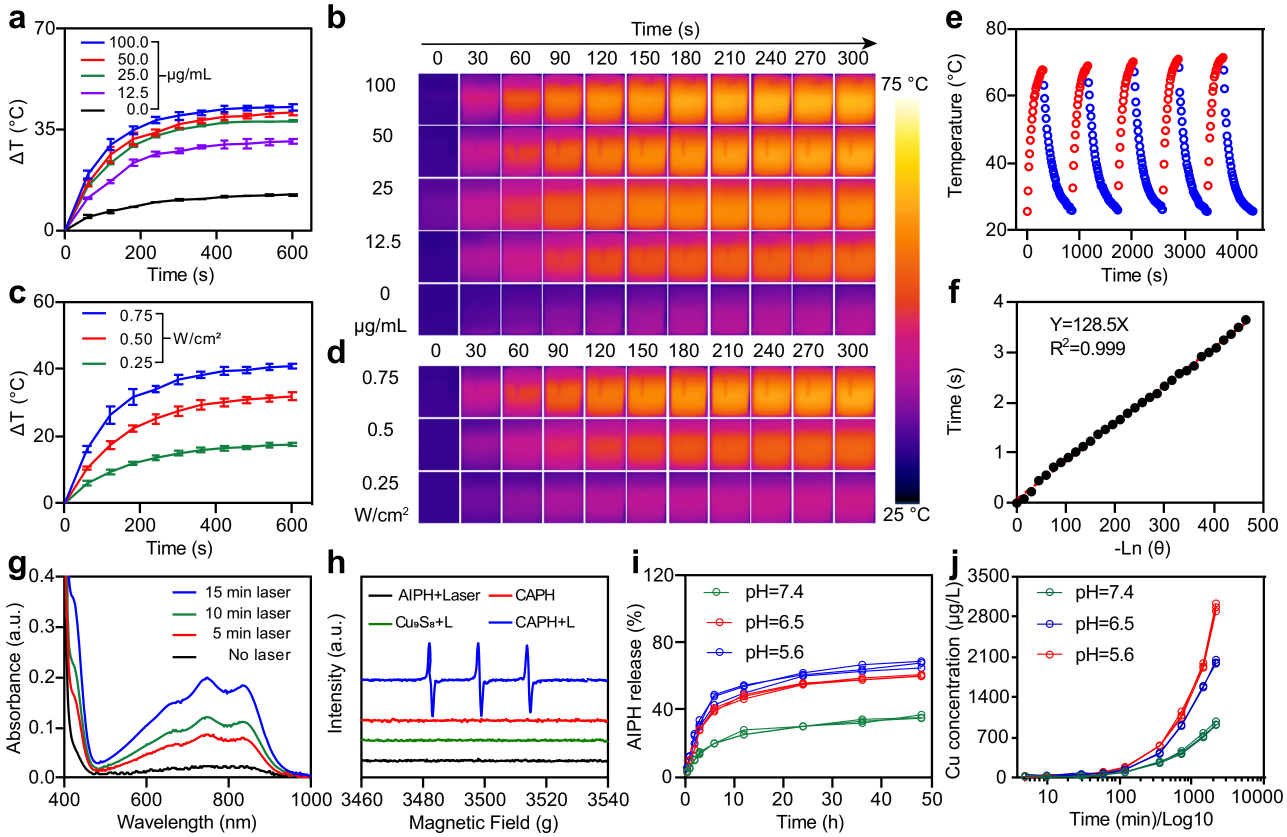

Fig. 3 | Photothermal, radical generation, and drug/copper ions release of CAPSH. **a**, **b** Temperature versus time curves and thermal imaging results of Cu_9S_8 (0–100 μg/mL) under 1064 nm laser irradiation (0.75 W/cm^2). Data were presented as the means ± SD ($n = 3$ independent experiments). **c**, **d** Temperature versus time curves and thermal imaging results of Cu_9S_8 at 100 μg/mL under 1064 nm laser irradiation (0.25–0.75 W/cm^2). Data were presented as the means ± SD ($n = 3$ independent experiments). **e** Temperature rise and fall curves of Cu_9S_8 irradiated repeatedly with a 1064 nm laser irradiation (0.75 W/cm^2). **f** Photothermal conversion efficiency curve of Cu_9S_8. **g** Free radical production was induced by irradiating CAPH at different times using a 1064 nm laser. **h** ESR spectra in AIPH, Cu_9S_8, and CAPH solutions irradiated with a 1064 nm laser using POBN as a spin-trapping agent. **i** AIPH release from CAPH in PBS at different pH (n=independent experiments). **j** Copper ions release of CAPSH in PBS at different pH ($n = 3$ independent experiments). Source data are provided as a Source Data file.

80 μg/mL, of CAPSH were chosen to investigate the combined impact of their treatment. At a concentration of 40 μg/mL (Fig. 4b), the survival rate of 4T1 cells remained above 80% without NIR laser exposure. However, under light exposure, the cell survival rate dropped to 22.1%. On the other hand, at an 80 μg/mL concentration of CAPSH (Fig. 4c), the survival rate of 4T1 cells was still above 48% without NIR laser irradiation. Nevertheless, under light exposure, the cell survival rate decreased to 15.3%. Additionally, we conducted toxicity tests on 3T3 and RAW cells using CAPSH and found that the cytotoxicity of CAPSH was lower at low concentrations (0–20 μg/mL), but significantly increased at high concentrations (100 μg/mL) (Supplementary Fig. 14).

We studied the uptake of CAPSH by 4T1 and 3T3 cells. CAPSH was added to the medium of 3T3 and 4T1 cells, and cells were co-cultured and collected at different time points (2, 4, and 8 h). ICP-MS analysis of copper content in the cells can be found in Supplementary Fig. 15, revealed that 4T1 cells uptake more CAPSH than 3T3 cells at the same time points. Flow cytometry further confirmed this finding (Fig. 4d). This indicated that due to the targeting effect of HA, CAPSH uptake was more pronounced in cancer cells than in normal cells. The release of the drug at the cellular level was demonstrated by detecting the fluorescence of DOX, and a large amount of DOX entered the cells within 6 h, showing that the hollow mesoporous structure of Cu_9S_8 was successful in achieving effective drug loading and release (Supplementary Fig. 16).

Furthermore, we investigated the generation of free radicals using DCFH-DA. As depicted in Fig. 4e, neither the control group nor the AIPH group demonstrated the capability to initiate free radical production. In contrast, the most intense green fluorescent signal was observed in 4T1 cells subjected to CAPH treatment followed by laser irradiation. This observation suggested that the photothermal impact of Cu_9S_8 facilitated the breakdown of AIPH, leading to the formation of alkyl radicals. The viability of 4T1 cells following various treatments was assessed through fluorescence imaging using calcineurin-AM/PI staining (Fig. 4f). In both the control and AIPH-treated groups, vibrant green fluorescence (indicating live cells) persisted even after laser irradiation, underscoring robust cell activity. In stark contrast, the CAPH and CAPSH treatment groups exhibited a considerable population of cells emitting red fluorescence (indicative of cell death) post laser irradiation. Notably, the CAPSH group displayed the highest observed cell mortality rate among the treatment groups. This observation underscored that a synergistic combination of multiple treatments could significantly enhance the efficiency of tumor cell eradication. The flow cytometry data showed that the cell necrosis rate in the CAPSH+Laser group was 40.8% higher than that in the control group (Fig. 4g). These results further confirmed that the CAPSH+Laser group had a great antitumor effect.

Mechanism of cell death mediated by CAPSH

Through bioinformatics analysis, we have discovered a significant upregulation in the expression levels of *ATP7A* and the copper-related apoptosis gene dihydrolipoamide *S*-acetyltransferase (DLAT) in breast invasive carcinoma (BRCA) compared to normal tissues (Fig. 5a, b). These findings suggest that breast cancer may exhibit sensitivity to copper apoptosis therapy, with high levels of *ATP7A* expression

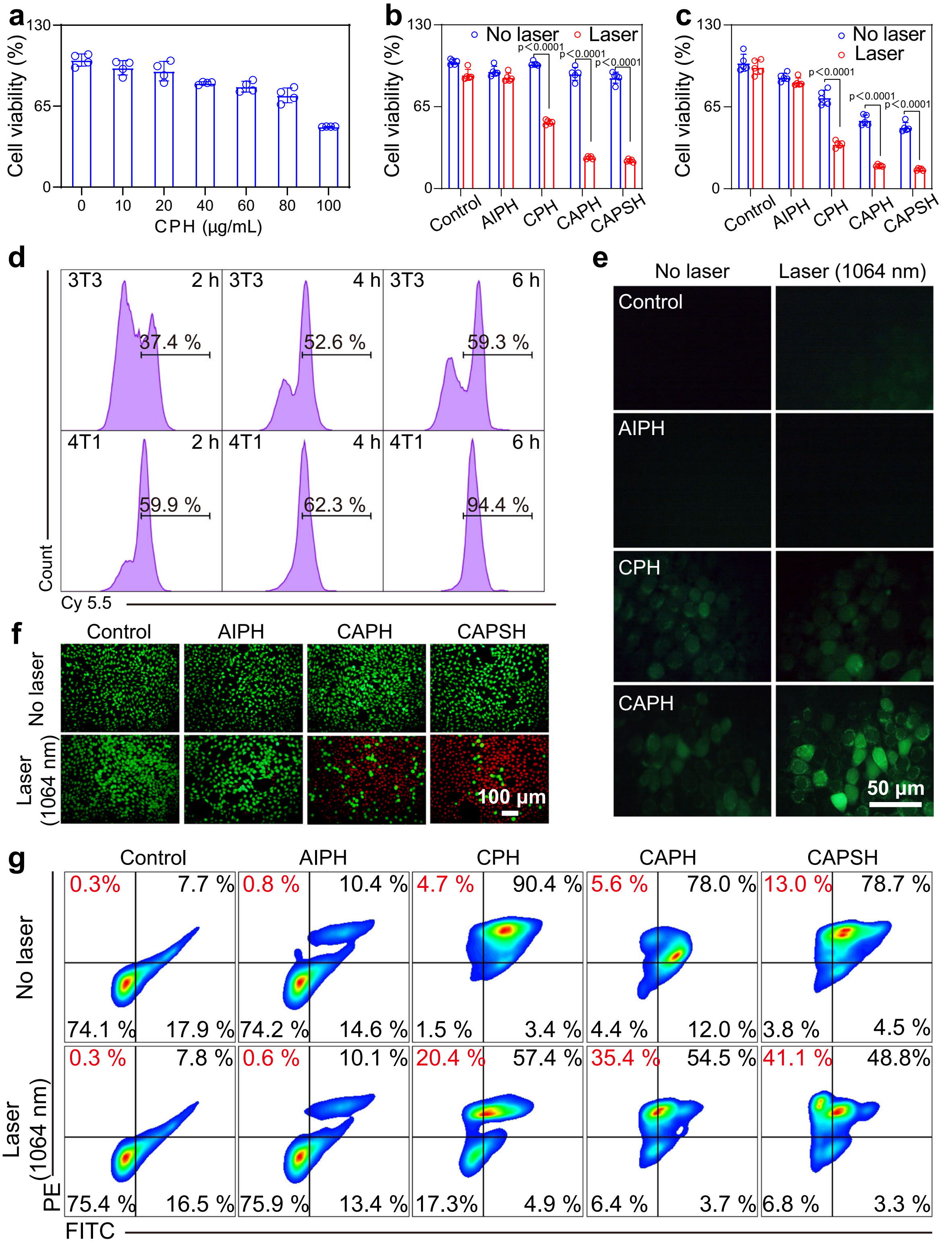

Fig. 4 | Therapeutic effects of the CAPSH at the cellular level. a MTT for CPH toxicity on 4T1 cells. Data were presented as the means ± SD ($n = 4$ independent experiments). **b**, **c** Cell survival of 4T1 cells after different treatments. The concentration of AIPH in (**b**) was 10 μg/mL, and the concentration of Cu_9S_8 in CPH, CAPH, and CAPSH was 40 μg/mL. Data were presented as the means ± SD ($n = 5$ independent experiments). The concentration of AIPH in (**c**) was 20 μg/mL, and the concentration of Cu_9S_8 in CPH, CAPH, and CAPSH was 80 μg/mL. Data were presented as the means ± SD ($n = 5$ independent experiments). **d** Flow cytometry was used to detect the intake of CAPSH by 3T3 and 4T1 cells at different time points. The gate strategy is shown in Supplementary Fig. 37. **e** Fluorescence images of intracellular free radicals. Images are representative of three independent experimental replicates. Scale bar: 50 μm. **f** Images of 4T1 cells co-stained with calcineurin-AM (green)/PI (red) after different treatments. Images are representative of three independent experimental replicates. Scale bar: 100 μm. **g** Flow cytometry for cell survival at 4T1 after different treatments. Images are representative of three independent experimental replicates. The gate strategy is shown in Supplementary Fig. 37. Significance between the two groups in (**b**, **c**) was assessed by unpaired two-tailed Student's *t*-test. Source data are provided as a Source Data file.

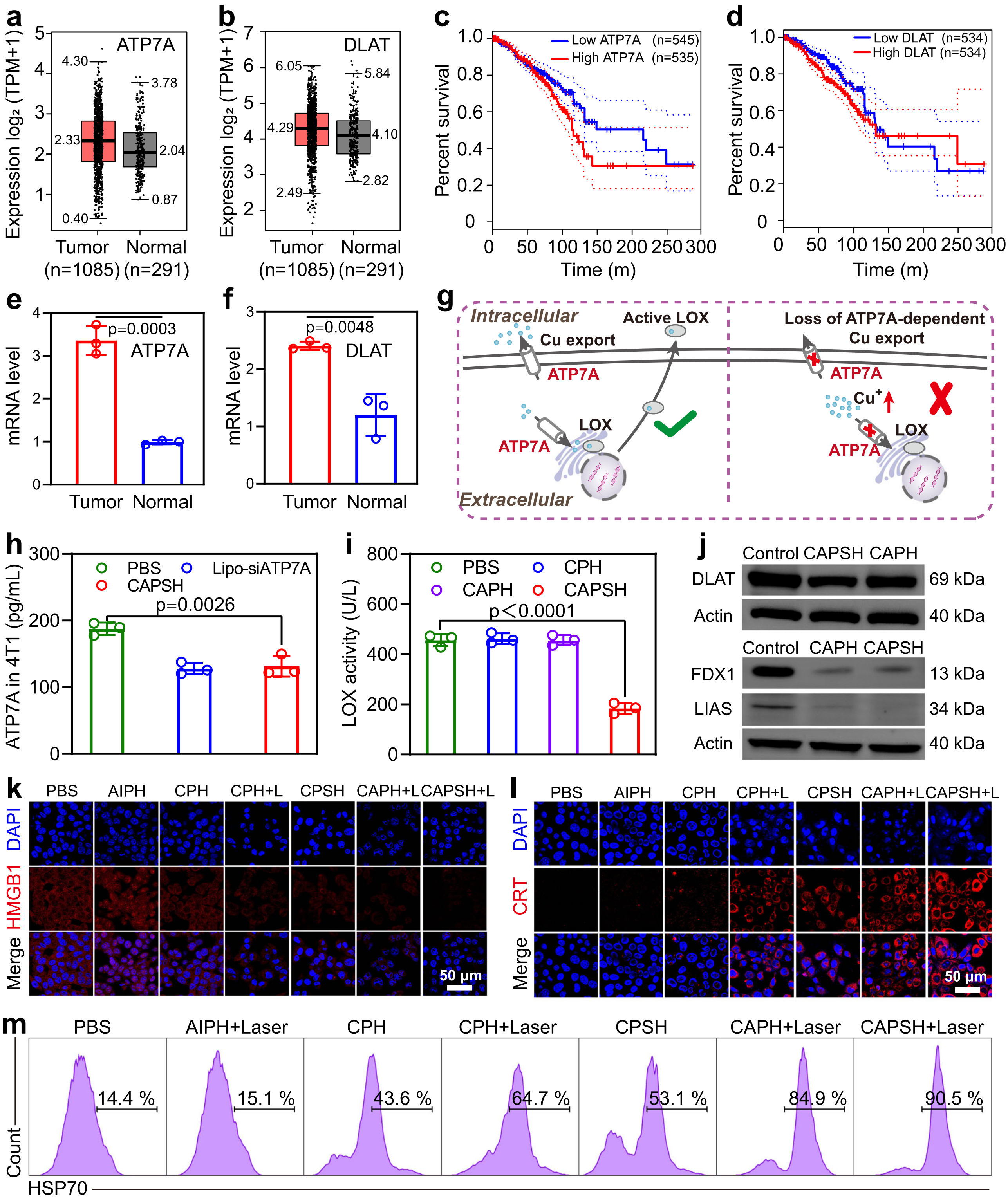

Fig. 5 | Mechanism of cell death mediated by CAPSH. **a** Bioinformatics analysis of *ATP7A* in BRCA. **b** Bioinformatics analysis of *DLAT* in BRCA. **c**, **d** Patient survival analysis of *ATP7A* and *DLAT* in BRCA. **e**, **f** mRNA levels of *ATP7A* and *DLAT* in 4T1 and 3T3 cells. Data were presented as the means ± SD ($n = 3$ independent experiments). **g** A functional model of ATP7A in tumor growth and metastasis. **h** Protein content of ATP7A in 4T1 cells after different treatments. Data were presented as the means ± SD ($n = 3$ independent experiments). **i** LOX activity of 4T1 cells after different treatments. Data were presented as the means ± SD ($n = 3$ independent experiments). **j** DLAT, FDX1, and LIAS protein levels after treatment of 4T1 cells with different samples. Images are representative of three independent experimental replicates. The samples of the same group were derived from the same experiment, and the gels/blots were processed in parallel. **k**, **l** Immunofluorescence analysis of the expression of HMGB1 and CRT in 4T1 cells after different treatments, DAPI was used to stain nuclei (blue). Images are representative of three independent experimental replicates. Scale bar: 50 μm. **m** Quantitative analysis of HSP70 expression in 4T1 cells after different treatments using flow cytometry. Images are representative of three independent experimental replicates. The gate strategy is shown in Supplementary Fig. 38. Significance between two groups in (**e**, **f**) was assessed by unpaired two-tailed Student's *t*-test, and between each of the multiple groups in (**h**, **i**) was calculated using one-way ANOVA. Source data are provided as a Source Data file. Figure 5g was created with BioRender.com released under a Creative Commons Attribution 4.0 International license (https://creativecommons.org/licenses/by/4.0/).

potentially exerting a negative regulatory effect on copper apoptosis. In addition, we observed higher survival in patients with lower levels of *ATP7A* and *DLAT* over 8 years and lower survival in patients with higher levels of *ATP7A* (Fig. 5c) and *DLAT* (Fig. 5d). PCR analysis further confirmed the high expression of *ATP7A* (Fig. 5e) and *DLAT* (Fig. 5f) in tumor tissues and their low expression in normal tissues. These results strongly indicated that a potentially promising approach to breast cancer treatment might involve the combined application of copper apoptosis therapy and *ATP7A* intervention.

Copper levels within the body were intricately regulated through a complex network. When intracellular copper concentrations became elevated, the copper transport protein ATP7A, situated in the trans-Golgi network, relocated to the plasma membrane and facilitates the efflux of copper (Fig. 5g)[8]. This mechanism served to avert the excessive accumulation of copper ions, a pivotal step in maintaining intracellular copper balance. Disturbing ATP7A's function enhanced the accumulation of intracellular copper ions, disrupting copper homeostasis. Simultaneously, ATP7A contributed copper ions to diverse copper-dependent enzymes. When its function was impaired, it could result in the dysfunction of multiple enzymes, subsequently affecting the organism's normal physiological processes. Research indicated that silencing *ATP7A* hampers LOX activity, thereby impeding the phosphorylation of focal adhesion kinase (FAK)[35]. LOX, an amine oxidase responsible for the oxidative deamination of lysine residues in collagen, interacted with epithelial-mesenchymal translational transcription factors, playing a role in tumor invasion and metastasis[36].

To explore CAPSH's potential for delivering siRNA into cells and silencing target genes, we initially examined the mRNA levels of *ATP7A* in 4T1 cells subjected to various treatments via fluorescence quantitative PCR experiments. Notably, the mRNA levels of *ATP7A* in the CAPSH-treated group exhibited a substantial reduction (Supplementary Fig. 17). Furthermore, we conducted a precise quantification of ATP7A using ELISA (Fig. 5h). The protein levels of ATP7A were significantly reduced in the CAPSH-treated group, indicating effective gene silencing. Additionally, we measured the activity of LOX in cells after different treatments. The results showed that CAPSH effectively inhibited LOX activity in 4T1 cells (Fig. 5i). Next, we investigated the effect of ATP7A deletion on cell migration by in vitro scratch assay (Supplementary Fig. 18). The CAPSH-treated group showed significantly weaker cell migration compared with the CPH- and CAPH-treated groups. The cell migration rate in the blank group was 91.7%, while in CAPSH, it was only 29.3% (Supplementary Fig. 19). It indicated that inhibition of ATP7A expression could suppress the migration and metastatic ability of tumors. Subsequently, extracting proteins from 4T1 cells enabled us to study the expression of copper toxicity-related proteins at the protein level through Western blotting experiments (Fig. 5j). We investigated the CAPSH-mediated copper death phenomenon by comparing the expression of relevant proteins in 4T1 cells after different sample treatments. The protein expressions of DLAT, ferredoxin 1 (FDX1), and lipoic acid synthetase (LIAS) were significantly decreased after CAPSH and CAPH treatments. And the expression of DLAT and LIAS in the CAPSH-treated group was lower than that in the more CAPH-treated group. This suggested that the knockdown of *ATP7A* by siRNA contributed to the enhancement of the copper death strategy.

We further investigated the accumulation of copper ions in 4T1 cells (Supplementary Fig. 20). The results showed that, compared to the control group, the copper ions content in the Lipo-siRNA group increased (cultured in a medium with low copper ions content). Additionally, the copper ions content in the CAPSH group was higher than in the CAPH group. The study demonstrated that when the *ATP7A* gene in tumor cells was knocked out, copper ions significantly accumulated within the cells. This accumulation significantly enhanced the copper-induced cell death effect, thereby achieving effective killing of tumor cells. More importantly, this copper-induced cell death (cuproptosis) was not limited to the direct killing of tumor cells but could also trigger immunogenic cell death (ICD). When ICD occurred, characteristic danger-associated molecular patterns (DAMPs) were exposed or released, including changes in calreticulin (CRT), high mobility group box 1 (HMGB1), heat shock protein 70 (HSP70), and adenosine triphosphate (ATP). Immunofluorescence results indicated (Fig. 5k, l) that 4T1 cells in the CPSH group significantly induced the release of HMGB1 from the nucleus and the surface exposure of CRT, exceeding the levels observed in the CPH group. Flow cytometry was used to quantitatively analyze the expression of HMGB1, CRT (Supplementary Fig. 21), and HSP70 (Fig. 5m). The results showed that the positive rate of HMGB1 in the CPSH group was 16.1% lower, the positive rate of CRT was 9.4% higher, and the positive rate of HSP70 was 20.2% higher than in the CPH group. The ATP content in the supernatant of the CPSH group was 1.48 times higher than that in the CPH group (Supplementary Fig. 22). Overall, *ATP7A* knockdown resulted in increased accumulation of intracellular copper ions and promoted ICD. CAPSH combination therapy had a significant effect on the promotion of ICD.

In vivo antitumor efficacy

In order to assess the safety profile of CAPSH, we conducted in vitro tests to examine the stability of CAPSH in the blood (Supplementary Fig. 23). The outcomes of the hemolysis assay revealed that even after 3 h of co-incubation with 100 μg/mL of CAPSH, the rate of erythrocyte hemolysis remained below 3%. This finding supported the favorable applicability of CAPSH for potential in vivo use. Based on the above experimental results, we established a subcutaneous injection of the 4T1 tumor-bearing Balb/c mouse model to evaluate the antitumor efficacy of CAPSH. The 4T1 tumor-bearing mice were randomly divided into six groups: PBS, AIPH + L, CAPH, Cu_9S_8 + Laser (Cu_9S_8+L), CAPH + L, and CAPSH + L. After 24 h of injecting different samples, the mice in the laser group were irradiated at the tumor sites using a near-infrared laser (1064 nm, 0.75 W/cm^2, 5 min) (Fig. 6a). Among them, the tumor volume of mice in the PBS and AIPH + L groups increased rapidly. The slow increase in the CAPH group was attributed to apoptosis induced by copper ions. Mice in the Cu_9S_8 + L, CAPH + L, and CAPSH + L groups exhibited significant tumor suppression under NIR laser irradiation (Fig. 6b–d). The treatment effect was most significant in the CAPSH + L group. The tumors of the mice were weighed after the treatment, which lasted for 25 days, and the weight of the tumors further supported this result (Fig. 6e). There were no significant changes in the body weight of all mice during the treatment, indicating that the samples had good biosafety (Fig. 6f). The temperature changes at the tumor sites of mice were monitored through thermal imaging, and there was no difference in the temperature changes at the tumor sites of the Cu_9S_8 + L and CAPSH + L groups 12 h after the injection of the samples into the tail vein. In contrast, 24 h after sample injection, the temperature at the tumor site in the CAPSH + L group was significantly higher than that in the Cu_9S_8 + L group, which was attributed to the targeting effect of HA resulting in a higher accumulation of CAPSH at the tumor site than that of Cu_9S_8 (Fig. 6g and Supplementary Fig. 24).

In addition, we observed the tumor tissues through Hematoxylin and Eosin (H&E) staining, terminal deoxynucleotidyl transferase-mediated dUTP nick end labeling (Tunel) assay, and immunofluorescence (IF) staining of Ki-67, respectively. As shown in Fig. 6h, H&E staining revealed the most severe apoptosis in the CAPSH + L group. The red fluorescence of Ki-67 was significantly reduced, while the green fluorescence of Tunel staining was significantly elevated, which further confirmed the highly efficient tumor-suppressing property of the combined treatment. We further evaluated the therapeutic effect of the combination therapy at the cytokine level. First, we examined the concentrations of TNF-α and IFN-γ in tumor tissues

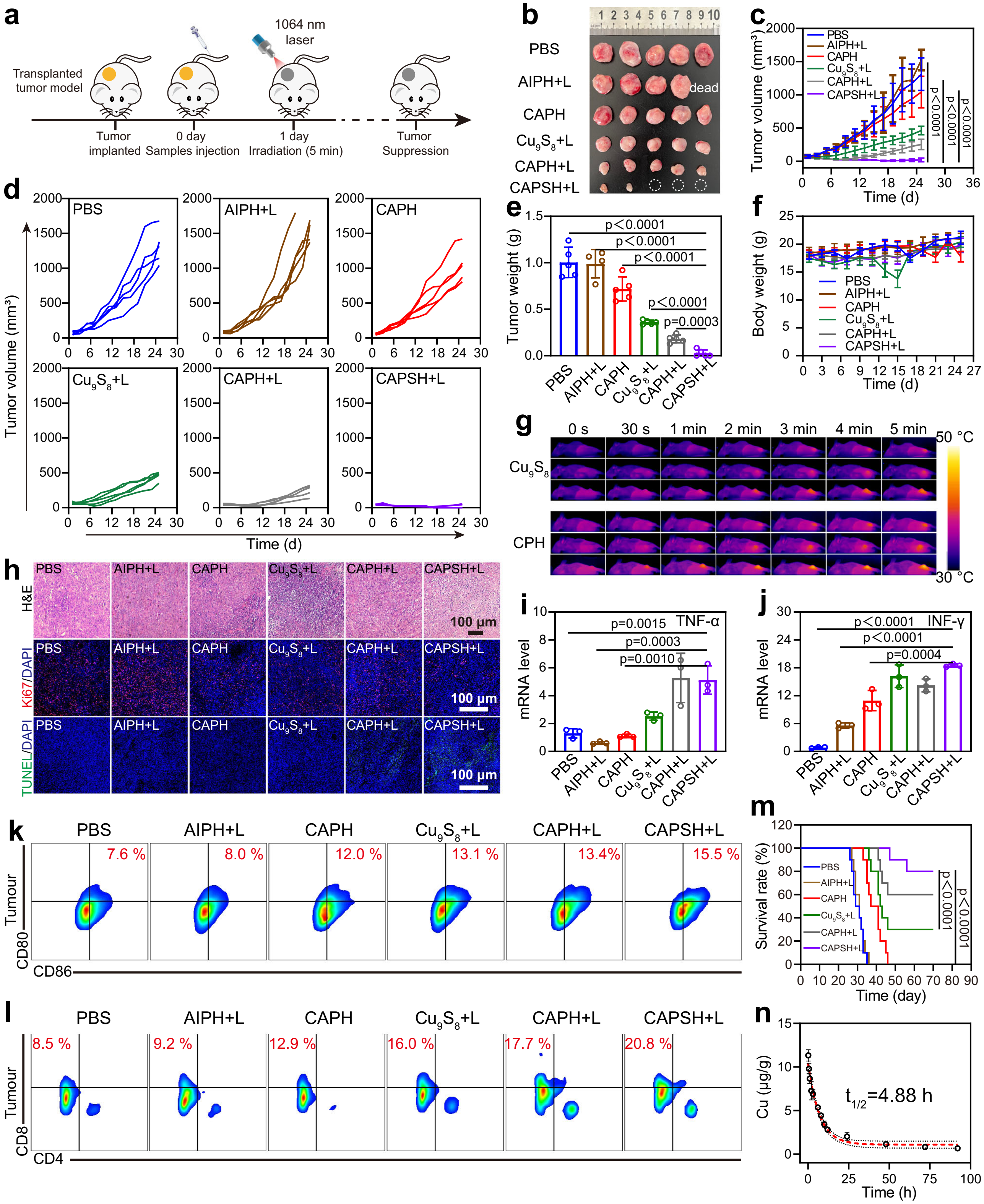

after different treatments. At the end of treatment, TNF-α (Fig. 6i) and IFN-γ (Fig. 6j) were significantly increased in the CAPSH + L group compared to the PBS group.

Next, we measured the expression levels of HMGB1 and CRT in tumor tissues as well as the changes in T cells and DC cells. The experimental results showed that in the CAPSH+Laser group, tumor cells significantly released a large amount of HMGB1 and CRT during the process of cell death (Supplementary Fig. 25 a, b). These immunogenic molecules not only acted as "danger signals" to activate the body's immune system but also served as potent adjuvants, guiding and promoting the recruitment and activation of T cells and DC cells in the spleen, lymph nodes, and tumor (Fig. 6k, l and Supplementary Fig. 25 c–e). In the tumor tissues, the percentage of DC cells and $CD8^+$ T cells significantly increased in the CAPSH + L treatment group, reaching 15.5 and 20.8%, respectively. It showed that the combination treatment had an immune-activating effect and contributed

Fig. 6 | Subcutaneous tumor model of breast cancer. a Transplanted tumor model in mice. **b** Photographs of representative tumors after different treatments, $n = 5$ mice per group. **c** Tumor volume after different treatments. Data were presented as the means ± SD ($n = 5$ mice per group). **d** Tumor volume change curves for each mouse after different treatments. **e** Tumor weights obtained after different treatments. Data were presented as the means ± SD ($n = 5$ mice per group). **f** Changes in body weight of mice after different treatments. Data were presented as the means ± SD ($n = 5$ mice per group). **g** Thermal imaging of Cu_9S_8 + L and CAPH + L groups at different times. **h** H&E sections and immunofluorescence staining (Ki-67 and Tunel) of tumor tissues from mice of different treatment groups. Images are representative of three biologically independent mice. Scale bar: 100 µm. **i** mRNA levels of TNF-α in different treated tumors. Data were presented as the means ± S.D. ($n = 3$ mice per group). **j** mRNA levels of IFN-γ in different treated tumors. Data were presented as the means ± SD ($n = 3$ mice per group). **k** Flow cytometry analysis of DC cells in the tumor. Images are representative of three independent experimental replicates. The gate strategy is shown in Supplementary Fig. 39. **l** Flow cytometry analysis of $CD8^+$ T cells in the tumor. Images are representative of three independent experimental replicates. The gate strategy is shown in Supplementary Fig. 39. **m** Survival rate of breast cancer model mice after different treatments, $n = 10$ mice per group. **n** Changes of Cu in blood over time. Data were presented as mean ± 95% confidence interval ($n = 3$ mice per group). The significance between each of the multiple groups in (**c**, **e**, **i**, **j**) was calculated using one-way ANOVA. Source data are provided as a Source Data file.

to tumor treatment. In addition, the CAPSH group exhibited the highest long-term survival rate (Fig. 6m).

Cu was used as a tracer to investigate the distribution and metabolism of CAPSH in the blood, major organs, and tumor sites in mice. The results indicated that CAPSH had a relatively long circulation time in the blood ($t_{1/2} = 4.88$ h), which was advantageous for the targeted transport of CAPSH to tumor sites (Fig. 6n). The distribution and metabolism of CAPSH in vivo showed time-dependent characteristics with different effects on different organs (Supplementary Fig. 26). In addition, the prolonged retention time of CAPSH in tumor tissues provided an effective therapeutic window.

In situ models closely resemble natural lesions histologically and cytologically as they develop in situ, mimicking the growth of tumor cells in their original location. To further investigate, we established an in situ breast cancer tumor model and treated tumor-mice using the same treatment as the transplanted tumor model (Fig. 7a). The therapeutic effect was assessed through the monitoring of tumor volume in the mice, as well as the weight of the tumors and the body weight of the mice. Among them, mice in the CAPH + L group and CAPSH + L group showed significant tumor inhibition (Fig. 7b–d). Tumor growth before and after treatment was monitored by bioluminescence of tumor cells expressing luciferase. As expected, the CAPH + L group and the CAPSH + L group showed the highest tumor inhibition efficiency during treatment, whereas none of the other treatments were effective in inhibiting tumor growth (Fig. 7e). After the treatment lasted for 14 days, the tumors of the mice were weighed, and the tumor weights further confirmed this result (Fig. 7f). There was no significant change in the body weight of all mice during the treatment period (Fig. 7g). We further evaluated the therapeutic effect of the combination therapy at the cytokine level. we examined the concentrations of TNF-α and IFN-γ in tumor tissues after different treatments. At the end of treatment, TNF-α (Fig. 7h) and IFN-γ (Fig. 7i) were significantly increased in the CAPSH + L group compared to the PBS group. Furthermore, the robust tumor-suppressive effects of the combination treatment were further validated through an array of investigative techniques. This included the examination of tumor tissues via H&E staining, Tunel assay, and (IF) staining for Ki-67, CD8, and CD4 markers (Fig. 7j). Finally, we evaluated the therapeutic effect of CAPSH by detecting the mRNA levels of *ATP7A* and the copper death-related genes *DLAT* and *FDX1* in tumor tissues after treatment. As shown in Fig. 7k, for CAPH, Cu_9S_8 + L, and CAPH + L, the mRNA level of *ATP7A* was substantially increased, probably due to the increase in intracellular copper ions concentration, which led to the increase in the expression of *ATP7A* to resist the copper death of tumor cells. In the CAPSH + L group, the mRNA level of *ATP7A* was substantially reduced, indicating that siATP7A had a certain silencing effect on *ATP7A*. mRNA levels of *LIAS* (Fig. 7l) and *FDX1* (Fig. 7m) in the CAPSH + L group were reduced to a certain extent compared with those of CAPH + L, indicating that inhibition of *ATP7A* could promote cuproptosis of tumor cells. In addition, we examined the changes of monovalent copper ions content in tumor tissues of mice after tail vein injection of PBS and CAPSH for 12 h. The results showed that the monovalent copper ions content in the tumor tissues was significantly increased after injection of CAPSH, and the fluorescence intensity was 1.9 times higher than that in the PBS group (Supplementary Fig. 27).

In order to further evaluate the biosafety of CAPSH application in vivo, we conducted blood routine, blood biochemistry, organ coefficient, and histological examinations of major organs after administering CAPSH injections to mice. The results of the experiments revealed that there were no significant changes in seven indices: white blood cells (WBC), red blood cells (RBC), hemoglobin (HGB), platelets (PLT), alanine aminotransferase (ALT), aspartate aminotransferase (AST), and urea nitrogen (UREA) (Supplementary Fig. 28). Organ coefficients were used to assess the relative health or damage of various organs. We weighed the organs of the mice and calculated the organ coefficients (Organ weight/body weight × 100%) (Supplementary Fig. 29). The results revealed that the spleen coefficients and liver coefficients of the mice in the PBS group were significantly higher compared to those in the CAPSH group. However, there was no significant difference in the coefficients of other organs. These findings suggest that the spleen and liver in the PBS group exhibited abnormal cells, leading to significant organ changes. H&E staining of the heart, liver, spleen, lungs, and kidneys' tissues of the mice were observed, and none of them exhibited significant changes in tissue structure, which further demonstrated the favorable biosafety of CAPSH (Supplementary Fig. 30).

Inhibition of metastasis and long-term immune memory

Encouraged by the excellent performance of CAPSH + Laser in knocking out ATP7A and stimulating antitumor immune response, we further evaluated its impact on long-term metastasis inhibition in mice (Fig. 8a). On the 60th day after treatment, whole lung tissue photos and H&E staining showed that the CAPSH + Laser group had the least number of metastatic nodules (Fig. 8b). Compared with the CPH group, the CPSH group significantly reduced the metastasis of 4T1 cells in the lungs, confirming the importance of ATP7A in tumor invasion and metastasis. In addition, CAPSH not only inhibited metastasis by inhibiting ATP7A, but also activated the immune system by inducing ICD, further inhibiting metastasis. The experiment showed that the positive rate of $CD4^+$ T cells in the spleen and lymph nodes was higher in the CAPSH group, indicating that CAPSH can induce and maintain the immune response of $CD4^+$ T cells, producing long-term immune memory. The changes in $CD8^+$ T cells in the CAPSH group were not as significant as in the short term, reflecting the dynamic adjustment of immune cells (Fig. 8c). The results indicate that CAPSH+Laser effectively inhibits long-term metastasis by inhibiting ATP7A and activating the immune system.

Safety evaluation of CAPSH

The main side effects of CAPSH might originate from the non-targeted release of copper ions, causing damage to normal tissues. Copper ions have an impact on the oxygenation ability and structural stability of hemoglobin, which may disrupt its function and affect overall

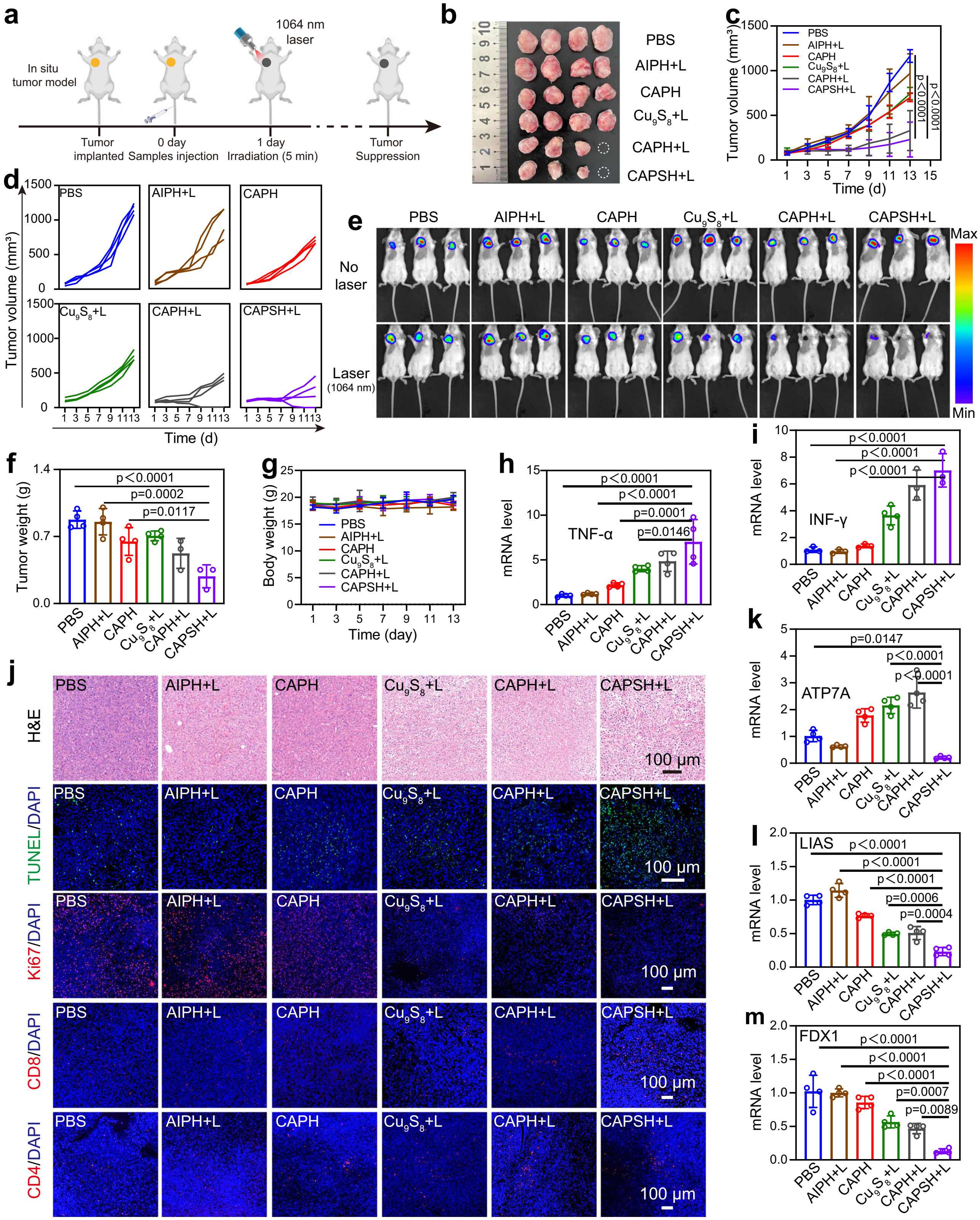

physiology. To demonstrate the low toxicity of CAPSH, we tested its interaction with hemoglobin. The results showed that there was no significant change in the absorption peak of hemoglobin at 415 nm, indicating that CAPSH had no significant effect on hemoglobin function (Supplementary Fig. 31). ICP-MS analysis of copper ions content in mouse serum can be found in the Supplementary Fig. 32, revealed that the copper ions concentration in the CAPSH group was 8.45 ± 0.89 μmol/L, which was higher than that in the PBS group, but did not exceed the safe concentration of 10–20 μmol/L. The Masson staining results showed no significant changes in collagen fibers, muscle tissue, cell nuclei, and other structures in the organs between the experimental group and the blank group, indicating that CAPSH did not cause damage to the organs (Supplementary Fig. 33).

Fig. 7 | In situ tumor model of breast cancer. **a** In situ tumor model in mice. **b** Photographs of representative tumors after different treatments, $n = 4$ mice per group. **c** Tumor volume after different treatments. Data are presented as the means ± SD ($n = 4$ mice per group). **d** Tumor volume change curves for each mouse after different treatments. **e** In vivo bioluminescence imaging of mice before and after treatment. **f** Tumor weights obtained after different treatments. Data were presented as the means ± SD ($n = 4$ mice per group). **g** Changes in body weight of mice after different treatments. Data were presented as the means ± SD ($n = 4$ mice per group). **h** mRNA levels of *IFN-γ* in different treated tumors. Data were presented as the means ± SD ($n = 4$ mice per group). **i** mRNA levels of *TNF-α* in different treated tumors. Data were presented as the means ± SD ($n = 4$ mice per group). **j** H&E sections and immunofluorescence staining (Tunel, Ki-67, CD8, and CD4) of tumor tissues from mice of different treatment groups. Images are representative of three biologically independent mice. Scale bar: 100 μm. **k** mRNA levels of *ATP7A* in different treated tumors. Data were presented as the means ± SD ($n = 4$ mice per group). **l** mRNA levels of *LIAS* in different treated tumors. Data were presented as the means ± SD ($n = 4$ mice per group). **m** mRNA levels of *FDX1* in different treated tumors. Data were presented as the means ± SD ($n = 4$ mice per group). The significance between each of the multiple groups in (**c**, **f**, **h**, **i**, **k**, **l**, **m**) was calculated using one-way ANOVA. Source data are provided as a Source Data file. Figure 7a was created with BioRender.com released under a Creative Commons Attribution 4.0 International license (https://creativecommons.org/licenses/by/4.0/).

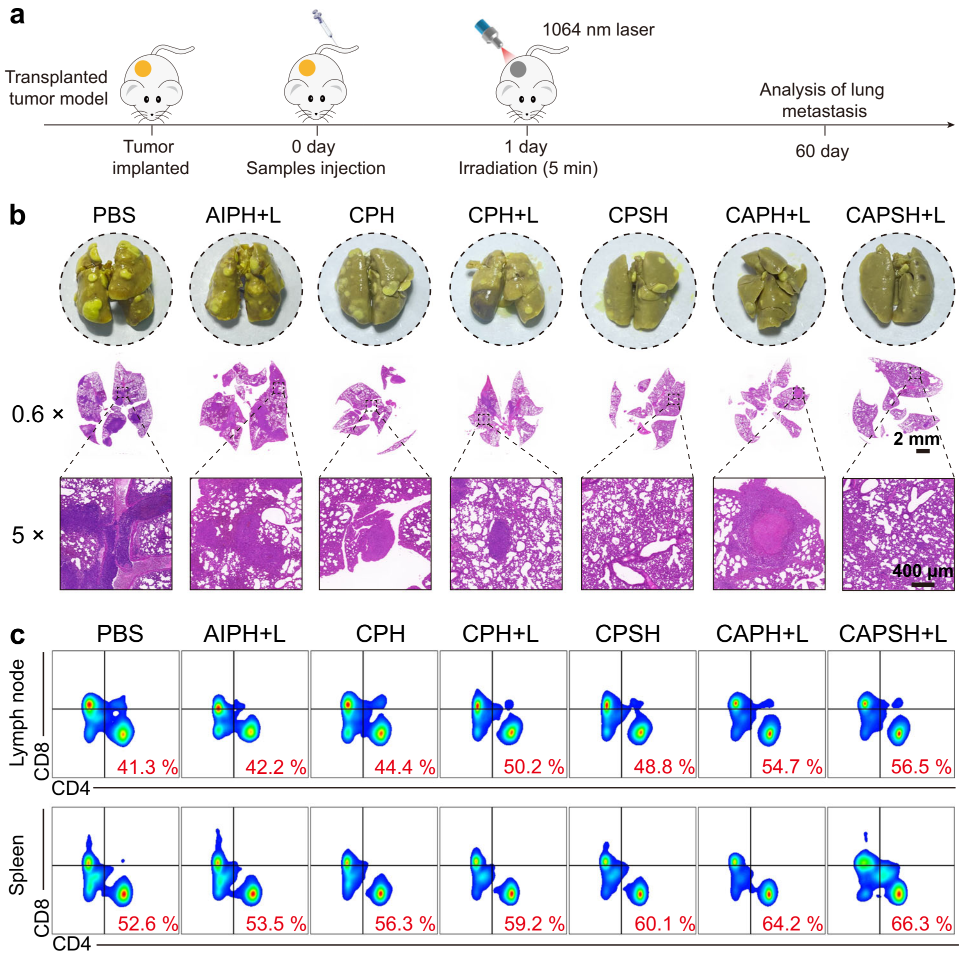

Fig. 8 | Inhibition of metastasis and long-term immune memory. **a** Schematic diagram of experimental design for transferring animals. **b** Representative photos of lung tissue and H&E staining of middle lung tissue in each group of mice. Images are representative of three biologically independent mice. Scale bar: 2 mm (top) and 400 μm (bottom). **c** Flow cytometry analysis of $CD4^+$ T cells in the lymph nodes and spleen. Images are representative of three biologically independent mice. Source data are provided as a Source Data file.

We investigated the acute and chronic toxicity of CAPSH in mice. Acute toxicity experiments have shown that doses of 80 mg/kg and above cause rapid death in mice, with the 70 mg/kg group dying within 4 days. The 60 mg/kg group had a survival rate of 50%, while the 30 mg/kg group showed no significant abnormalities, with a survival rate of 100%. Chronic toxicity experiments showed that mice at doses of 30 and 15 mg/kg exhibited PLT reduction and abnormal elevation of liver and kidney function indicators on the first day (Supplementary Figs. 34, 35). However, by the seventh day, these indicators returned to normal, indicating that the mice had the ability to self-repair after experiencing early acute liver and kidney injury. The experimental results indicate that a dose of 15 mg/kg is safe.

Utilizing proteomics, we conducted a comparative analysis to discern alterations in the proteome composition and the expression profiles of proteins in tumor tissues between the control and CAPSH treatment groups. Our objective was to ascertain whether CAPSH intervention modulates immune responses linked to metal ions beyond copper ions. Through meticulous examination of proteomics data and the graphical representation of differential protein expression via histograms and volcano plots, we identified a total of 627 proteins exhibiting differential expression, comprising 253 upregulated and 374 downregulated proteins (Supplementary Fig. 36a, b). Subsequently, we screened metal ion-related proteins (e.g., ion channel proteins, matrix metalloproteinases, and metal chaperonins) from these 627 differential proteins and displayed them in a Wayne diagram (Supplementary Fig. 36c). We then proceeded to perform a KEGG pathway enrichment analysis on the 149 differentially expressed proteins that were associated with metal ions, revealing that 29 of these proteins were intricately connected to the immune system (Supplementary Fig. 36d). Further elucidation of the proteins that intersect both metal ion biology and immune system involvement was achieved through a heat map representation of their fold changes (Supplementary Fig. 36e). Note that, upon functional annotation, it was observed that these differentially expressed proteins, which are associated with both metal ions and immune mechanisms, did not exert a significant influence on the immune modulation pertinent to oncotherapy. Consequently, our findings suggest that the CAPSH intervention did not elicit additional metal-related immune responses at the tumor site.

Discussion

In summary, we had successfully constructed a copper-based nanoplatform (CAPSH) for the treatment of breast cancer. Mesoporous Cu_9S_8 nanoparticles with photothermal effect was used as a delivery platform and copper reservoir, effectively delivering a large amount of copper ions, AIPH, and SiRNA to the breast cancer region. In the near-infrared II wavelength light (1064 nm) could not only release a large amount of copper ions through photothermal conversion to cause disintegration, but also the alkyl radicals generated by AIPH effectively killed local tumor cells. By introducing siRNA, the expression of ATP7A protein was successfully suppressed, thereby enhancing the sensitivity of tumor cells to copper ions, and further improving the occurrence of cuproptosis. Additionally, siRNA also helped inhibit tumor growth and metastasis by suppressing the activity of LOX. The mouse model of in situ breast tumors verified that the enhancement of cuproptosis effectively activated immunogenic death in this tissue region based on the release of tumor cell antigens, elevated the immune system response at the end of the treatment, and effectively inhibited tumor recurrence. This nanoplatform integrally enabled precise targeting of the tumor region, elevated the onset of cuproptosis, inhibited tumor cell self-regulatory mechanisms, and effectively activated the immune response. In summary, we proposed a therapeutic strategy that both promoted the occurrence of copper death and inhibited the self-regulation of tumor cells, combining the deep photothermal effect based on near-infrared II illumination as well as the generation of alkyl radicals to achieve a multidimensional and efficient treatment for breast tumors, and optimizing the application of cuproptosis in tumor therapy.

Methods

Ethical statement

All animal experiments were approved by the Animal Experimentation Ethics Committee of Huazhong University of Science and Technology (IACUC Number: S904).

Animals

Female Balb/c mice (6-8 weeks old, 18–20 g) were purchased from Beijing Vital River Laboratory Animal Technology Co., Ltd. Mice were housed in an animal facility under constant environmental conditions (room temperature, 22 ± 1 °C; relative humidity, 40–70%; and 12 h light-dark cycle), and all mice had free access to food and water. Tumor volume was calculated as 0.5 × (length × width × width). To minimize animal discomfort, according to the Guideline of Assessment for Humane Endpoints in Animal Experiments (Certification and Accreditation Administration of the P. R. China, RB/T 173-2018), in general experiments, the tumor burden should not exceed 5% of the animal's normal body weight; in therapeutic experiments, it should not exceed 10% of the animal's body weight (10% indicated that the diameter of the subcutaneous tumor on the back of a 25 g mouse reached 17 mm). At the end of the mouse experiments, mice were euthanized according to animal welfare standards (euthanasia of all animals was performed using isoflurane in small animal anesthetics).

Materials

Polyvinylpyrrolidone (PVP), copper chloride dihydrate ($CuCl_2$), sodium sulfide nonahydrate ($Na_2S{\cdot}9H_2O$), 2,2′-azinobis(3-ethylbenzothiazoline -6-sulfonic acid ammonium salt) (ABTS), α-(4-pyridine-*N*-oxide)-*N*-tert butylnitrone (POBN), 2,2′-azobis[2-(2-imidazolin-2-yl)propane] dihydrochloride (AIPH), and 3-(4,5)-dimethylthiahiazo(-z-y1)-3,5-di-phenytetrazoliumromide (MTT) was purchased from Shanghai Aladdin Biochemical Technology Co., Ltd (Shanghai, China). Sodium hydroxide (NaOH), hydrazine hydrate solution ($NH_2NH_2 \cdot xH_2O$), ethanol absolute, dimethyl sulfoxide (DMSO) isopropanol, sodium chloride, sodium dodecyl sulfate, anhydrous methanol, concentrated nitric acid, and hydrochloric acid was purchased from Sinopharm Chemical Reagent Co., Ltd (Shanghai, China). Calcein acetoxymethyl ester (Calcein AM), propidium iodide (PI), reactive oxygen species assay Kit, BCA protein assay Kit, SDS-PAGE sample loading buffer 5X, hydrophobic polyvinylidene fluoride, (PVDF), penicillin−streptomycin, RNase-free dd H_2O, 4% paraformaldehyde fix solution and tween-20 was purchased from Shanghai Biyuntian Biotechnology Co., Ltd (Shanghai, China). Polyacrylamide hydrochloride (PAH) was purchased from Anhui Zesheng Technology Co., Ltd (Anhui, China). Hyaluronic acid (HA) was purchased from Sigma-Aldrich (Shanghai, China). RNA isolater, HiScript III All-in-one RT SuperMix Perfect for qPCR Kit and Taq Pro Universal SYBR qPCR Master Mix Kit was purchased from Vazyme Biotech Co., Ltd (Nanjing, China). ECL Chemiluminescence Substrate Kit was purchased from Beijing Labgic Technology Co., Ltd (Beijing, China). Pancreatin was purchased from Gino Saber Biotechnology Co., Ltd (Zhejiang, China). Omni-Easy™ One-Step PAGE Gel Fast Preparation Kit was purchased from Shanghai Yaenzyme Biopharmaceutical Technology Co., Ltd (Shanghai, China). Fetal bovine serum (FBS) was purchased from Zhejiang Tianhang Biotechnology Co., Ltd (Zhejiang, China). PBS and DMEM was purchased from Thermo Fisher Scientific Co., Ltd (Shanghai, China). Phenylmethanesulfonyl fluoride, Tris(hydroxymethyl)methyl aminomethane, and Glycine was purchased from Beijing Kehbio Technology Co., Ltd (Beijing, China). All solutions were prepared using ultrapure water from the Milli-Q system (≥18.20 M Ω).

Cell lines

Mouse breast cancer cells (4T1: CRL-2539), mouse embryonic fibroblasts (NIH-3T3: CRL-1658), and mouse monocyte macrophage leukemia cells (RAW264.7: TIB-71) cell line was obtained from Wuhan Saikangte Biotechnology Co., Ltd. Mouse breast cancer cells-luciferase labeled (4T1-LUC: CRL-2539-LUC2) cells was cell line obtained from Wuhan service Biotechnology Co., Ltd. All three cells were cultured in DMEM medium containing 10% fetal bovine serum, 100 U/mL penicillin, and 0.1 mg/mL streptomycin. All cell lines in this study get tested without mycoplasma contamination. Each cell line was morphologically confirmed according to the information provided by the cell-source center, and the main 4T1, NIH-3T3, and RAW264.7 cell lines were authenticated with short tandem repeat (STR) analysis (Supplementary Tables 2–4).

Synthesis of Cu_9S_8

Weighing 480 mg of polyvinylpyrrolidone was dissolved in 50 mL of ultrapure water, 200 μL of $CuCl_2$ solution (0.5 M) was added and stirred for 5 min, then 50 mL of NaOH solution at pH = 9, and 16 μL of hydrazine hydrate (85%) were added to form a bright yellow Cu_2O suspension. After stirring for 5 min, 400 μL of Na_2S solution (1.33 M) was added, and the reaction was carried out at 60 °C for 2 h. At the end of the reaction, the solution was washed by centrifugation with a water/ethanol solution with a volume ratio of 2:1 at 10,000×*g* three times. The copper ions content was determined by ICP-MS and the mass of Cu_9S_8 was calculated to be 3.5 mg.

Synthesis of CPH, CAP, CAPH, CAPSH

To 1 mL of Cu_9S_8 (1 mg/mL) solution, 0.1 mg of PAH was added and stirred for 12 h. The solution was washed by centrifugation three times. Adding 1 mg of HA and stirring for 8 h. Centrifuging and washing three times to obtain CPH. To 1 mL of Cu_9S_8 (1 mg/mL), adding 4 mg of AIPH and stirring for 12 h. Adding 0.1 mg of PAH and stir for 12 h. Centrifuging and washing three times to obtain CAP. About 1 mg of CAP is stirred with 1 mg of HA for 8 h. Centrifuging and washing three times to obtain CAPH. CAPS was obtained by incubating 0.12 mg of CAP with 3 μg of siRNA at 4 °C for 2 h. About 0.12 mg of HA was added and stirred for 8 h. The sample was washed by centrifugation three times to obtain CAPSH. The sequence of siATP7A is as follows: 5′-CCCGAGUGAUAGCAGAGUUUAdTdT-3′, The siATP7A was synthesized by Jinkairui Biotechnology Co., Ltd.

Photothermal properties of Cu_9S_8

About 200 μL of Cu_9S_8 at different concentrations (12.5, 25, 50, and 100 μg/mL) were taken in the wells of removable enzyme labeling plates, and the samples were irradiated with a 1064 nm laser at 0.75 W/cm^2 for 5 min, and the temperature changes of the samples with the laser irradiation were recorded with an infrared thermography camera. The same method was used to determine the temperature change of Cu_9S_8 at a concentration of 100 μg/mL at different power densities (0.25, 0.50, and 0.75 W/cm^2), and three parallels were set up for each sample. To test the photothermal stability of the probes, 200 μL of Cu_9S_8 at a concentration of 100 μg/mL was placed in the wells of a removable enzyme plate. The samples were then irradiated using a 1064 nm laser at 0.75 W/cm^2 for 5 min. After irradiation, the samples were cooled for 5 min, and the temperature change was recorded using an infrared thermography camera. The photothermal conversion efficiency of Cu_9S_8 was calculated using Eq. (1):

$$\eta = \frac{hs(T_{max} - T_{surr}) - Q_{Dis}}{I(1 - 10^{-A_{1064}})} \tag{1}$$

$hs = mc/\tau$; $Q_{\mathrm{Dis}} = hs \times (T_{\mathrm{max\ of\ water}} - T_{\mathrm{surr}})$, T_{max} represents the peak temperature at which Cu_9S_8 undergoes heating, T_{surr} denotes the surrounding ambient temperature, T_{max} of the water signifies the maximum temperature reached during the water heating process. The mass of the solution is denoted by "*m*", the specific heat capacity of water is represented as "*c*", the laser power is expressed as "*I*", and the absorption value at 1064 nm is indicated as A_{1064}.

Detection of free radicals

AIPH underwent thermal decomposition, resulting in the production of alkyl radical groups that reacted with ABTS to form $ABTS^{+\bullet}$. The solution containing a mixture of CAPH and ABTS was exposed to a 1064 nm laser with a power density of 0.75 W/cm^2 for 5, 10, and 15 min. After centrifugation, the UV absorption spectrum of the solution was measured using UV-vis absorption spectroscopy in the range of 400–1000 nm. To determine the type of free radicals generated, we mixed 150 μL of AIPH, Cu_9S_8, and CAPH with 100 mM POBN. The illuminated group was then irradiated with a NIR laser with a power density of 0.75 W/cm^2 for 5 min. On the other hand, the non-illuminated group was mixed for 5 min and then directly detected. After the different treatments, we measured the ESR signals of the samples at 25 °C using an ESR spectrometer.

Encapsulation rate and drug release studies of AIPH

In a 1 mL solution of Cu_9S_8 (1 mg/mL), 4 mg of AIPH was introduced and stirred for 12 h. Subsequently, 0.1 mg of PAH was added, and the mixture was stirred for an additional 12 h. The absorption value of the supernatant at 365 nm was determined through centrifugation, and the mass of AIPH was calculated based on the standard curve. The encapsulation rate was calculated using Eq. (2):

$$\begin{aligned} &\mathit{Encapsulation\ rate}\\ &= \frac{(\mathit{mass\ of\ initially\ added\ AIPH}) - (\mathit{mass\ of\ AIPH\ in\ the\ supernatant})}{\mathit{mass\ of\ initially\ added\ AIPH}} * 100\% \end{aligned} \tag{2}$$

The CAPH was dialyzed using a 500 Da dialysis bag, and the pH of the dialysate was adjusted to 5.4, 6.5, and 7.4. At regular intervals, the external fluid of the dialysis bag was sampled, and the UV absorption value was measured. The sample was then returned to the dialysis bag, and this process was repeated until the absorption value remained constant. The content of AIPH in the external fluid of the dialysis bag was calculated using the standard curve of AIPH.

Release of copper ions

A solution of Cu_9S_8 (1 mg/mL) was placed in a dialysis bag. The pH of the dialysate was then adjusted to 5.4, 6.5, and 7.4. Samples were collected at specific time intervals of 5, 10, 30 min and 1, 2, 6, 12, 24, 36 h. The amount of copper ions presented in the solution was measured using ICP-MS.

ICP-MS testing conditions

Sample pretreatment: After weighing the tumor tissues, homogenize them using a tissue homogenizer and digest them in concentrated nitric acid until the solution is clear and transparent. Standard curve: Prepare a standard curve using a standard solution of known concentration (the concentration of the standard curve is 10, 20, 40, 60, 80 μg/L). Instrument setting: set the element to be detected as copper, select the standard mode, and optimize the parameters. The plasma power was between 1000–1600 W. Set the argon flow rate at 0.8–1.2 L/min. Testing: The sample was fed into the plasma through the feeding system, and the signal intensity of the characteristic ions was recorded. Data analysis: The standard curve was plotted according to the counts per second (cps) of the standard solution versus concentration. The concentration of the elements in the sample is calculated by comparing the signal intensity of the sample with the standard curve.

Cytotoxicity assay

4T1 cells were inoculated in 96-well plates, with ~5×10^3 cells per well and 5 parallels per group. Once the cells were fully attached to the wall, different concentrations of CPH (0, 10, 20, 40, 60, 80, and 100 μg/mL) were added. After 12 h, the medium was removed, and the cells were washed with PBS three times. Then, 100 μL of 1 mg/mL MTT solution was added to each well. After 4 h, the medium and MTT solution were aspirated out, and 100 μL of DMSO was added to each well. The plate was shaken for 20 min to ensure even distribution. Subsequently, the absorption at 490 nm of each well was measured using an enzyme marker to determine cell viability.

In vitro combination therapy experiments

The 4T1 cells were uniformly inoculated in 96-well plates with ~5×10^3 cells per well. There were five parallel groups in each group, and they were cultured for 24 h. The cells were then treated with AIPH, CPH, and CAPH, respectively, for 12 h. After that, the medium was removed, and the cells were washed three times with PBS. In the illumination group, the cells were exposed to a 1064 nm laser at a power density of 0.75 W/cm^2 for 5 min. Then, the medium was added back, and the incubation continued for 6 h. Subsequently, 100 μL of 1 mg/mL MTT solution was added to each well. After 4 h, the MTT solution was aspirated out, and 100 μL of DMSO was added to each well. The 96-well plate was then placed on a shaking table and shaken uniformly for 20 min. Finally, the absorption of each well at 490 nm was measured with an enzyme marker to calculate the cell viability.

The 4T1 cells were inoculated homogeneously in 24-well plates with ~1×10^5 cells per well and cultured for 24 h. The old medium was discarded, and the cells were treated with AIPH, CPH, and CAPH, respectively, for 12 h. After being washed three times with PBS, the light group was exposed to a laser with a power density of 0.75 W/cm^2 at 1064 nm for 5 min and then cultured for 4 h. The cells were co-stained using the Calcein AM/PI assay and observed under inverted fluorescence microscopy.

Cell uptake

ICP-MS detection. Adding CAPSH to the culture medium of 3T3 and 4T1 cells and co-culture. Collect the cells at 2, 4, and 8 h. After counting, nitric acid was added for digestion, and ICP-MS was used to measure the copper content within the cells.

Flow cytometry detection. Loading Cy5.5 onto CAPSH and adding it to the culture medium of 3T3 and 4T1 cells. Co-culture and collecting the cells at 2, 4, and 8 h. Using flow cytometry to detect the fluorescence intensity of Cy5.5.

Detection of free radicals in cells

The 4T1 cells were uniformly inoculated in 24-well plates with ~1×10^5 cells per well and cultured for 24 h. The old medium was then discarded, and the cells were treated with AIPH, CPH, and CAPH, respectively, for a duration of 12 h. The intracellular content of reactive oxygen species was assessed using the DCFH-DA reactive oxygen species detection kit.

In vitro detection of ICD activation

Sterile coverslips were placed in a 12-well culture plate, and 4T1 cells were seeded and cultured for 24 h. After different treatments, the cells were incubated for an additional 6 h. Subsequently, the medium was removed, and the cells were washed twice with PBS. The 4T1 cells were then fixed with 4% paraformaldehyde and permeabilized with 0.1% Triton X-100. Next, the cells were blocked with 5% BSA at room temperature for 20 min. Following blocking, the cells were incubated overnight at 4 °C with anti-HMGB1, anti-HSP70, and anti-CRT antibodies. After overnight incubation, the cells were washed three times with PBS and incubated with secondary antibodies at room temperature for 1 h. Finally, the cells were washed three times with PBS, and the coverslips were carefully mounted on slides with DAPI antifade mounting medium for confocal fluorescence imaging and flow cytometry detection. 4T1 cells were seeded in a 12-well plate and cultured for 24 h. After different treatments, the cells were incubated for an additional 6 h. Subsequently, the ATP content in the culture medium was detected using an ATP assay kit.

Copper distribution in tumors and organs

To study the distribution of copper in tumors and organs, 30 tumor-bearing mice were selected. Each mouse was administered an intravenous injection of 150 μL of CAPSH (2 mg/mL) through the tail vein. At the following time points: 0.5, 1, 2, 4, 6, 8, 12, and 24 h, as well as 5 and 15 days post-injection, three mice were euthanized at each time point. The heart, liver, spleen, lungs, kidneys, and tumor tissues were then harvested. After weighing the tissues, each sample was homogenized in a tissue grinder with 400 μL of PBS. Subsequently, 5 mL of concentrated nitric acid was added to the samples, which were then stored in the dark for several hours. Once the samples were completely digested at 120 °C in a digestion apparatus until the solution was clear and transparent, the copper content was measured using ICP-MS.

Blood half-life study

For the study of blood half-life, 150 μL of CAPSH (2 mg/mL) was administered intravenously to three BALB/c mice via the tail vein. Blood samples were collected at the following time points: 10 min, 30 min, 1, 2, 3, 4, 6, 8, 10, 12, 24, 48, 72, and 96 h post-injection. Each blood sample was then digested with concentrated nitric acid until the solution was completely clear. The concentration of copper in the blood was determined using ICP-MS.

RNA extraction

The adherent cells were washed three times with PBS after different treatments, 1 mL of RNA isolator was added, and the cells were blown down and collected in a centrifuge tube. Next, 200 μL of chloroform was added to the solution. The mixture was vigorously shaken for 15 s to form an emulsion and then left to stand on ice for 5 min. After that, the solution was centrifuged at 12,000×*g* for 15 min at 4 °C. The upper aqueous phase was aspirated into a new centrifuge tube. To this tube, an equal volume of pre-cooled isopropanol was added. The mixture was mixed upside down and left to stand on ice for 10 min. Subsequently, the tube was centrifuged at 12,000×*g* for 10 min at 4 °C. Usually, a white precipitate is visible at this stage. The supernatant was removed, and 1 mL of 75% ethanol was added. The tube was inverted several times and left at room temperature for 3–5 min. Then, it was centrifuged at 12,000×*g* for 5 min at 4 °C, and the supernatant was discarded. The precipitate was dried for 2–5 min, and an appropriate amount of RNase-free dd H_2O was added to dissolve it. Finally, the ratios of A_{206}/A_{230} and A_{260}/A_{280} were measured using a micro-spectrophotometer. The primer sequences used in quantitative polymerase chain reaction experiments are provided in Supplementary Table 5.

Detection of intracellular protein expression

The cell precipitate was collected, washed three times with PBS, and the liquid was aspirated. Protein lysate (RIPA: PMSF = 1000:1) was added to the cell precipitate and thoroughly mixed. It was then placed on an ice bath and lysed for 1 h. Finally, it was centrifuged at 12,000×*g*, 4 °C for 5 min. The protein concentration in the supernatant was determined by the BCA Protein Concentration Assay Kit and mixed with loading buffer solution thoroughly, placed in heating denaturation at 98 °C for 10 min, and placed in the refrigerator at −20 °C for storage. The protein samples were separated by SDS-PAGE gel electrophoresis and transferred to the PVDF membrane. The membrane was blocked with 5% BSA in TBST for 1 h at room temperature and immunoblotted with primary antibody overnight at 4 °C. The membrane was then washed three times with TBST and incubated with HRP-labeled secondary antibody at room temperature for 1 h. Finally, the protein bands were visualized using the Enhanced Chemiluminescence (ECL) Substrate Kit.

In vivo safety evaluation

To assess the biosafety of CAPSH, blood samples (400 μL per mouse) were obtained from the heart after the completion of treatment. A portion of 300 μL was placed in a procoagulant tube containing separating gel and centrifuged for 10 min. The resulting supernatant was used for liver and renal function analysis, including AST, ALT and UREA. An additional 100 μL was collected in an anticoagulant tube for routine blood tests, such as RBC, WBC, PLT, and HGB measurements. Furthermore, the heart, liver, spleen, lung, and kidney of the mice were collected, weighed, fixed in 4% paraformaldehyde, dehydrated, embedded, and sectioned for H&E staining and histopathological examination using a light microscope.

In vivo antitumor efficiency

Two tumor models were utilized to evaluate the effectiveness of antitumor treatment in vivo. The subcutaneous tumor model was established by injecting ~1×10^6 4T1 cells per mouse into the lower right back of Balb/c mice. The in situ tumor model was created by injecting ~1×10^6 4T1-LUC cells per mouse into the first pair of mammary glands in the chest of Balb/c mice. Once the tumor volume reached

80–100 mm^3, the mice in the subcutaneous tumor model were randomly divided into six groups (seven mice per group): PBS, AIPH + L, Cu_9S_8 + L, CAPH, CAPH + L, CAPSH + L. Similarly, the mice in the in situ tumor model were randomly divided into six groups (four mice per group). Each group was administered 150 µL of different samples through the tail vein, with a dosage of 15 mg/kg for Cu_9S_8 in the Cu_9S_8 + L, CAPH, CAPH + L, CAPSH + L group, and 12 mg/kg for AIPH in the AIPH + L, CAPH, CAPH + L, CAPSH + L group. After 24 h of sample injection, the light group irradiated the tumor with a laser having a wavelength of 1064 nm and a power density of 0.75 W/cm^2 for 5 min. The changes in body weight and tumor volume were recorded every other day. Tumor growth monitoring in mice with in situ tumor models using an animal fluorescence imager.

Statistics and reproducibility

Data were expressed as mean ± SD. Significance between the two groups was assessed by unpaired two-tailed Student's *t*-test, and between each of the multiple groups was calculated using one-way ANOVA. Values with $P < 0.05$ were considered significant. Exact *p* values were provided accordingly in the figures. All the statistical analyses were performed using GraphPad Prism (9.5.0). In this study, the sample size was determined based on prior experimental experience and standard practices. We did not use statistical methods to predetermine the sample size. During data analysis, no data were excluded. We have provided a detailed description of the experimental methods to ensure that other researchers can replicate the experiment and verify the reproducibility of the results. Flow-cytometry data were analyzed with FlowJo (ver. 10.8.1). ImageJ (ver. 1.4.3.67) were used to analyze fluorescent grayscale. Alpha EaseFC 4.0 was used to analyze the WB. Confocal images were analyzed with FluoView31S (ver.2.3.1.163).

Reporting summary

Further information on research design is available in the Nature Portfolio Reporting Summary linked to this article.

Data availability

All data generated or analyzed during this study are included in this published article, its Supplementary Information file, and the Source Data file. The bioinformatics and survival analysis of ATP7A and DLAT in BRCA patients data in Fig. 5a–d can be found in [https://figshare.com/articles/figure/Data_sources_for_Figures_5a-d/27626775]. Source data are provided with this paper.

References

1. Bedoui, S., Herold, M. & Strasser, A. Emerging connectivity of programmed cell death pathways and its physiological implications. *Nat. Rev. Mol. Cell Biol.* **21**, 678–695 (2020).
2. Fan, J. X. et al. Engineered bacterial bioreactor for tumor therapy via fenton-like reaction with localized H_2O_2 generation. *Adv. Mater.* **31**, 1808278 (2019).
3. Tsvetkov, P. et al. Copper induces cell death by targeting lipoylated TCA cycle proteins. *Science* **375**, 1254–1261 (2022).
4. Xu, Y. Z. et al. An enzyme-engineered nonporous copper (I) coordination polymer nanoplatform for cuproptosis-based synergistic cancer therapy. *Adv. Mater.* **34**, 2204733 (2022).
5. Chen, K. et al. An intelligent cell-derived nanorobot bridges synergistic crosstalk between sonodynamic therapy and cuproptosis to promote cancer treatment. *Nano Lett.* **23**, 3038–3047 (2023).
6. Chan, L. et al. Cuproptosis-driven enhancement of thermotherapy by sequentially response $Cu_{2-x}Se$ via copper chemical transition. *Adv. Funct. Mater.* **33**, 2302054 (2023).
7. Xue, Q. et al. Copper metabolism in cell death and autophagy. *Autophagy* **19**, 2175–2195 (2023).
8. Shanbhag, V. et al. ATP7A delivers copper to the lysyl oxidase family of enzymes and promotes tumorigenesis and metastasis. *Proc. Natl Acad. Sci. USA* **116**, 6836–6841 (2019).
9. Gao, W. et al. Elesclomol induces copper-dependent ferroptosis incolorectal cancer cells via degradation of ATP7A. *Mol. Oncol.* **15**, 3527–3544 (2021).
10. Gallas, A., Alexander, C., Davies, M., Puri, S. & Allen, S. Chemistry and formulations for siRNA therapeutics. *Chem. Soc. Rev.* **42**, 7983–7997 (2013).
11. Zhang, J. et al. Syphilis mimetic nanoparticles for cuproptosis-based synergistic cancer therapy via reprogramming copper metabolism. *Int. J. Pharm.* **640**, 123025 (2023).
12. Kim, B., Park, J. & Sailor, M. Rekindling RNAi therapy: materials design requirements for in vivo siRNA delivery. *Adv. Mater.* **31**, e1903637 (2019). J.
13. Eygeris, Y., Gupta, M., Kim, J. & Sahay, G. Chemistry of lipid nanoparticles for RNA delivery. *Acc. Chem. Res.* **55**, 2–12 (2021).
14. Lei, Y. et al. Gold nanoclusters-assisted delivery of NGF siRNA for effective treatment of pancreatic cancer. *Nat. Commun.* **8**, 15130 (2017).
15. Han, X. X. et al. Reversal of pancreatic desmoplasia by re-educating stellate cells with a tumor microenvironment-activated nanosystem. *Nat. Commun.* **9**, 3390 (2018).
16. Jin, X. K. et al. Orchestrated copper-based nanoreactor for remodeling tumor microenvironment to amplify cuproptosis-mediated anti-tumor immunity in colorectal cancer. *Mater. Today* **68**, 108–124 (2023).
17. Zhao, Y. et al. Design and synthesis of cancer-cell-membrane-camouflaged hemoporfin-Cu_9S_8 nanoagents for homotypic tumor-targeted photothermal-sonodynamic therapy. *J. Colloid Interf. Sci.* **637**, 225–236 (2023).
18. Liu, X. et al. Multifunctional doxorubicin@hollow-Cu_9S_8 nanoplatforms for photothermally-augmented chemodynamic-chemo therapy. *J. Colloid Interf. Sci.* **615**, 38–49 (2022).
19. Cheng, Y. et al. An intelligent biomimetic nanoplatform for holistic treatment of metastatic triple-negative breast cancer via photothermal ablation and immune remodeling. *ACS Nano* **24**, 15161–15181 (2020).
20. Niu, S. et al. Hollow mesoporous silica nanoparticles gated by chitosan-copper sulfide composites as theranostic agents for the treatment of breast cancer. *Acta Biomater.* **126**, 408–420 (2021).
21. Sheng, Y. Y. et al. Construction of PEGylated chlorin e6@CuS-Pt theranostic nanoplatforms for nanozymes-enhanced photodynamic-photothermal therapy. *J. Colloid Interf. Sci.* **645**, 122–132 (2023).
22. Yan, T. et al. Synergistic photothermal cancer immunotherapy by Cas9 ribonucleoprotein-based copper sulfide nanotherapeutic platform targeting PTPN2. *Biomaterials* **279**, 121233 (2021).
23. Wei, X. D. et al. Biomimetic nano-immunoactivator via ionic metabolic modulation for strengthened NIR-II photothermal immunotherapy. *Small* **16**, e2304370 (2023).
24. Xu, W. et al. Localized surface plasmon resonances in self-doped copper chalcogenide binary nanocrystals and their emerging applications. *Nano Today* **33**, 100892 (2020).
25. Zou, Q., Pan, H., Zhang, X. & Zhang, C. Flower-like Cu_9S_8 nanocatalysts with highly active sites for synergistic NIR-II photothermal therapy and chemodynamic therapy. *J. Mater. Chem. B* **11**, 4740–4751 (2023).
26. Yang, J. et al. Supramolecular nanomaterials based on hollow mesoporous drug carriers and macrocycle-capped CuS nanogates for synergistic chemo-photothermal therapy. *Theranostics* **10**, 615–629 (2020).
27. Zheng, Z. et al. Starch capped atomically thin CuS nanocrystals for efficient photothermal therapy. *Small* **17**, 2103461 (2021).

28. Zhang, W. et al. Light-responsive core-shell nanoplatform for bimodal imaging-guided photothermal therapy-primed cancer immunotherapy. *ACS Appl. Mater. Interfaces* **12**, 48420–48431 (2020).
29. Li, Q. et al. A HMCuS@MnO_2 nanocomplex responsive to multiple tumor environmental clues for photoacoustic/fluorescence/magnetic resonance trimodal imaging-guided and enhanced photothermal/ photodynamic therapy. *Nanoscale* **12**, 12508 (2020).
30. Zhou, S. et al. Multifunctional self-assembly with NIR light-activated cascade effect for improving local treatment on solid tumors. *ACS Appl. Mater. Interfaces* **14**, 14087–14096 (2022).
31. Silvio, D. D. et al. Self-assembly of poly(allylamine)/siRNA nanoparticles, their intracellular fate and siRNA delivery. *J. Colloid Interf. Sci.* **557**, 757–766 (2019).
32. Choi, K. Y. et al. Hyaluronic acid-based activatable nanomaterials for stimuli-responsive imaging and therapeutics: beyond CD44-mediated drug delivery. *Adv. Mater.* **34**, 1803549 (2019).
33. Fan, J. X. et al. Antibody engineered platelets attracted by bacteria-induced tumor-specific blood coagulation for checkpoint inhibitor immunotherapy. *Adv. Funct. Mater.* **31**, 2009744 (2021).
34. Fan, J. X., Niu, M. T., Qin, Y. T., Sun, Y. X. & Zhang, X. Z. Progress of engineered bacteria for tumor therapy. *Adv. Drug Deliv. Rev.* **185**, 114296 (2022).
35. Li, X. Q., Combs, J. D., Salaita, K. & Shu, X. K. Polarized focal adhesion kinase activity within a focal adhesion during cell migration. *Nat. Chem. Biol.* **19**, 1458–1468 (2023).
36. Barker, H. E., Cox, T. R. & Erler, J. T. The rationale for targeting the LOX family in cancer. *Nat. Rev. Cancer* **12**, 540–552 (2012).

Acknowledgements

This work was supported by the National Natural Science Foundation of China (Grant Nos. 52103319, 62375093, 51803158, 62305121, and 82373104), the China Postdoctoral Science Foundation Funded Project (Grant No. 2023T160247), Technology Innovation Program of Hubei Province (2024BCB058), and Beijing Bethune Charitable Foundation (2023-YJ-041-J-008). We thank the Analytical and Testing Center (HUST), the Research Core Facilities for Life Science (HUST) for the help of measurement. Many thanks to Elabscience Biotechnology Co. Ltd. for assisting in the detection of cuproptosis-related indicators.

Author contributions

M.G., J.-X.F. and X.-T.X. designed and prepared the materials. M.G., Y.L., and B.Z. performed the in vitro experiments. M.G., M.-W.M., K.C. and S.C. performed the in vivo experiments. M.G., W.C., J.-X.F., B.L. and Y.-D.Z. wrote the paper. All authors discussed the results and agreed on the final version of the paper. M.G., K.C. and X.-T.X. are acknowledged for their equal contributions to this article.

Competing interests

The authors declare no competing interests.

Additional information

Supplementary information The online version contains supplementary material available at https://doi.org/10.1038/s41467-024-54469-7.

Correspondence and requests for materials should be addressed to Bo Liu, Jin-Xuan Fan or Yuan-Di Zhao.

Peer review information *Nature Communications* thanks Xiao Zhao, and the other, anonymous, reviewer(s) for their contribution to the peer review of this work. A peer review file is available.

Reprints and permissions information is available at http://www.nature.com/reprints